The Pennsylvania State University

The Graduate School

John and Willie Leone Family Department of Energy and Mineral Engineering

MICROTOMOGRAPHY IMAGING OF FLUID DISTRIBUTION AND INTERFACIAL AREA IN BEAD PACKS UNDER VARIABLE AXIAL LOADING

A Thesis in

Energy and Mineral Engineering

by

Samet Konya

Submitted in Partial Fulfillment
of the Requirements
for the Degree of

Master of Science

August 2015

The thesis of Samet Konya was reviewed and approved* by the following:

Zuleima T. Karpyn
Associate Professor of Petroleum and Natural Gas Engineering
Thesis Advisor

Eugene Morgan
Assistant Professor of Petroleum and Natural Gas Engineering

Turgay Ertekin
Professor of Petroleum and Natural Gas Engineering
Head of the Department of Energy and Mineral Engineering

Luis F. Ayala
Associate Professor of Petroleum and Natural Gas Engineering
Associate Department Head for Graduate Education

*Signatures are on file in the Graduate School

ABSTRACT

Reservoir stress and compaction play an important role in understanding transport phenomena in porous media. It is known that changing stress conditions has an impact on distribution and interaction of immiscible phases in the subsurface. However, there is limited pore-scale experimental data to examine the effect of compaction on porous media transport properties, which in turn requires further validation. The purpose of this work is to investigate macro- and pore-scale properties of granular packs with changing axial stress conditions using a synthetic water-wet porous medium. In this study, we provide a general framework to explore the effect of compaction on the porosity, permeability, relative permeability, surface area and interfacial area in a simplified porous medium. A specially designed core holder was used to exert simultaneous axial and radial stress on a glass bead column. Immiscible fluids (water and soltrol) were injected through the packing to reach equilibrium residual wetting and non-wetting phase saturation conditions. Then, variation in porosity, permeability, relative permeability, residual distribution of phases and interfacial area were monitored in accordance with different axial loadings ranging from 50 to 350 psig. X-ray microtomography (microCT) was used to monitor three-dimensional changes in pore structure. It was observed that axial loading resulted in minor changes in pore structure and residual fluid distributions. Average porosity dropped from 44.83% to 42.66%, whereas absolute permeability dropped from 30.39 to 25.11 Darcy with increasing axial loading. Scattered meniscus interfacial area (a^{wn}) values were found at irreducible wetting-phase saturation while similar a^{wn} values were found at residual non-wetting phase saturation as axial load

increased. Thus, a^{wn} is more sensitive to changes in pore structure at irreducible wetting-phase saturation. In dynamic conditions, contact angle hysteresis have an impact on the shape of curvature of the interface between immiscible phases and its affect is proven experimentally in the literature. In most of those experimental studies, meniscus interfacial areas (a^{wn}) at different saturation points on drainage curve were reported to be higher than that of imbibition which could be explained by contact angle hysteresis. In the present study, similarly, higher a^{wn} values were found at the end of drainage cycles than that of imbibition. However, this behavior cannot be attributed to contact angle hysteresis, alone. Our findings provide evidence that contact angle hysteresis affects pore-scale displacement mechanisms which consequently lead to changes in final saturation states. It should also be noted that the sensitivity of a^{w} to change in pore structure is higher than that of a^{n} at high wetting-phase saturations. However, a^{w} and a^{n} are in a good agreement at low wetting-phase saturations with linear approximations obtained from solid specific surface areas and saturations.

TABLE OF CONTENTS

LIST OF FIGURES

LIST OF TABLES

ACKNOWLEDGEMENTS

I would like to thank my advisor Dr. Zuleima T. Karpyn for motivating and encouraging me throughout this study. I am grateful Turkish Petroleum Corporation (TPAO) for giving me this great opportunity and I would like to express my gladness to my spouse for being patient and supporting me all the time.

I also want to express my appreciation to my lab mates Nrjor Chakraborty, Botros Abdelmalek and our lab technician Tim Stecko for their valuable friendship and assistance. If they had not helped me, I would not have done it.

I dedicate this thesis to my newborn son, Mirac.

Samet Konya

Chapter 1 : Introduction

Numerous investigations in recent years have focused on understanding multiphase fluid flow in porous media in the subsurface. As a result, transport phenomena has received remarkable attention due to its importance in fluid migration, oil and gas production and hydrocarbon recovery. In oil and gas reservoirs, reservoir pressure decreases through the process of reservoir depletion, thus inducing changes in net stress conditions (Nagel 2001). Reduction in reservoir pressure may result in reservoir compaction and it plays a significant role in the petroleum and natural gas industry (Nagel 2001; Holt et al. 2004). Compaction may supply pressure support to reservoir; however it may affect reservoir parameters like permeability in a negative way. (Geertsma 1973; Settari 2002). On the whole, compaction is remarkable for hydrocarbon production especially from unconsolidated reservoirs and depends upon effective stress, thickness and compressibility of the reservoir (Nagel 2001; Settari 2002). However, there is still limited experimental data to validate the effect of reservoir compaction and it needs to be further investigated. Also, few studies have focused on pore-scale investigations which could be vital to examine the effects of reservoir compaction (Geertsma 1973). In the present study, macro and micro-scale properties were investigated by conducting laboratory scale experiments at variable axial load conditions using a synthetic water-wet porous medium.

X-ray microtomography (microCT) is a non-invasive imaging method which enables researchers to analyze the inner structure of a material using high resolution

images (Landis & Keane 2010; Marques & Appoloni 2015). In recent years, there has been an increased interest in the use of X-ray microCT to visualize granular media (Landry et al. 2011; Blunt et al. 2013; Wildenschild & Sheppard 2013; Georgiadis et al. 2013; Marques & Appoloni 2015). Uses of X-ray microCT in the oil and gas industry are attracting prevalent interest because it helps to generate three dimensional structure of pore space efficiently (Karpyn et al. 2010).

The aim of this study is to gain further understanding of the effect of compaction at the pore-scale. The experiments presented in this study use a synthetic unconsolidated porous medium made of glass beads in order to investigate fundamental relationships between pore structure and fluid distribution according to variation in pore structure. A sequence of drainage and imbibition experiment was carried out by injecting immiscible fluids (water and soltrol) through bead packing at different axial loadings. The entire bead column was scanned with X-ray microCT scanner and three dimensional, high resolution images were evaluated using Avizo Fire 8.0 imaging software. The images were then used to make indirect measurements of classical macroscale properties such as porosity, permeability and residual fluid saturations in addition to surface and interfacial areas. Those properties were studied at both irreducible wetting and residual non-wetting phase saturations under different axial load conditions and are expected to, not only provide insights into the effect of axial loading and pore compaction, but also serve as robust calibration tool for pore-scale flow models.

Chapter 2 : Literature Review

Transport in porous media is of great significance in the context of transport in geologic formations, oil and gas reservoirs, hydrogeology and geosciences. Knowledge of flow mechanisms and the physics associated with it are essential to better understand transport phenomena (Jamaloei & Kharrat 2010). Hence, researchers attempted to study these through experiments and computer generated simulations. Being able to understand the properties that describe the transport underground is critical to be able to derive useful numerical models. These properties include basic macroscale properties of porosity and permeability, as well as pore-scale properties such as interfacial area, tortuosity, capillary pressure, etc. Due to the fact that it is quite difficult to obtain accurate pore structure of a porous medium, numerical pore-scale models are developed to represent porous media (e.g. predictive models). The numerical models incorporate pore network models (Blunt 2001; Valvatne et al. 2003; Joekar-Niasar & Majid Hassanizadeh 2011; Bultreys et al. 2015), smoothed particle hydrodynamics (Tartakovsky & Meakin 2006; Bandara et al. 2013), and Lattice Boltzmann models (Hazlett & Vaidya 2002; Porter et al. 2009; Boek & Venturoli 2010).

Experimental studies allow researchers to gain insight into flow mechanisms as well as observe the changes in macroscale properties quantitatively in porous medium. Synthetic experimental models have been built to study these flow mechanisms and the data generated from them can be used for pore-scale modelling or other explicit forms of modelling for validation purposes. Some of these models are based on simplistic representations like in this study.

Over the last few decades, a considerable amount of research has focused on understanding fundamental flow mechanisms in geologic formations. (Lenormand et al. 1983; Saputelli et al. 1998; Culligan et al. 2006; Li et al. 2006). Lenormand et al. 1983 conducted a pore level experiment to investigate the impact of capillarity on displacement efficiency. Saputelli et al. 1998 proposed a pore level experimental study which aims to provide insight into the role of gravity forces in a porous medium of variable microscale characteristics.

Killough 1976 presented a reservoir simulation method including the impact of capillary pressure and relative permeability hysteresis. He defined transition curves between drainage and imbibition curve in order to examine the success of simulation depending on those hystereses. Hassanizadeh & Gray 1993 were the first to suggest that capillary pressure was not only a function of saturation such that it must be evaluated with meniscus interfacial area (a^{wn}) as a 3D surface in lieu of classic 2D P_c-S_w curves. Culligan et al. 2006 studied interfacial areas between immiscible fluids (oil and water) in a syntetic water-wet porous medium. They scanned a bead column during drainage and imbibition (under dynamic conditions) at different saturations. From this, they investigated which pore-scale properties could be the source of possible dissimilarities in interfacial areas when oil was used instead of air in the same system (Culligan et al. 2004). They observed a consistent result with the literature that the meniscus interfacial areas were first rising to its highest value and then decreased according to wetting-phase saturation for both cases. Karpyn et al. 2010 made a comprehensive oil blob analysis by scanning a glass bead column at residual fluid saturations using X-ray microCT. They also investigated interfacial areas at the end of drainage and imbibition. Landry et al.

2011 focused on residual fluid distributions in a bead packing including acrylic beads after oil and water injections. They compared their results with Karpyn et al. 2010 mentioned above. In doing so, they investigated how and which pore-scale properties are influenced by wetting affinities of those media using X-ray microCT. They obtained similar $a^{wn} - S_w$ curves as Karpyn et al. 2010 but the highest numerical value of a^{wn} for water-wet medium was higher than that of oil-wet medium. Furthermore, they found the highest a^{wn} values at low wetting-phase saturations for both cases, which supports previous similar experiments. In addition, they calculated the number and surface area of residual fluid blobs after injections and demonstrated that both were considerably higher in oil-wet media because of the difference in wetting preferences of those two porous media.

Pore-scale studies are quite important as a foundation for larger scale models. The transport properties that are needed for representation of underground flow models are highly determined by pore-scale characteristics of that porous medium (Culligan et al. 2006). Pore space morphology and the physics associated with it assist in understanding the properties which drive the models that are used to understand oil and gas reservoirs. Recent studies focused on understanding the pore-scale phase interactions within porous medium by performing experiments using sands (Dutta et al. 2013), rock samples (Olivier et al. 2005; Jamaloei & Kharrat 2010) and simplistic representations (Landry et al. 2011; Larpudomlert et al. 2013; Georgiadis et al. 2013; Naghavi & Kibbey 2014; Marques & Appoloni 2015). Iassonov et al. 2009 made a comprehensive classification of pore-scale investigations in terms of methodology, segmentation type and properties explored (Figure 2.1).

Reference	Scanner	Resolution (μm)	Material	Segmentation	Properties
Ahrenholz et al. [2008]	SYN	11	sand	manual, 3D	LB simulations
Al-Raoush and Willson [2005]	SYN	5.8–23	glass beads, sand	adaptive, 3D	porosity, pore properties
Al-Omari and Masad [2004]	IND	146–293	asphalt	manual, 2D	hydraulic conductivity
Carminati et al. [2007]	IND	145	soil	thresholding, 3D	hydraulic conductivity
Culligan et al. [2006]	SYN	7.5	glass beads	thresholding, 3D	interfacial area
Jassogne et al. [2007]	MED	300	soil	thresholding, 2D	macroporosity
Jones et al. [2007]	SYN	6.8	sediments	adaptive, 3D	pore properties
Kaestner et al. [2006]	MED	36	soil	thresholding, 3D	root distribution
Kaestner et al. [2008]	SYN	6	aggregates	adaptive, 3D	porosity, permeability
Kutay et al. [2007]	IND	800	soil	manual, 2D	hydraulic conductivity
Lee et al. [2008]	M-IND	20	soil	thresholding, 2D	pore size distribution
Lehmann et al. [2006]	M-IND, SYN	3.5–70	glass beads, sand	manual, 3D	liquid distribution
Luo et al. [2008]	M-IND	5	soil	manual, 3D	preferential flow
Monga et al. [2008]	M-IND	11	soil	manual, 3D	pore space properties
Nunan et al. [2006]	SYN	4.4	aggregates	thresholding, 2D	porosity, shape
Okabe and Blunt [2004]	M-IND	10	sandstone	manual, 2D	hydraulic conductivity
Peth et al. [2008]	SYN	3.2–5.4	aggregates	adaptive, 3D	pore properties
Pierret et al. [2002]	MED	400	soil	adaptive, 2D	macropore properties
Prodanović et al. [2007]	SYN	5	sandstone	adaptive, 3D	phase distribution
Reed et al. [2006]	M-IND	11.8	sand	adaptive, 3D	particle shape
Sander and Gerke [2007]	IND	–	soil	manual, 2D	preferential flow patterns
Schaap et al. [2007]	SYN	17	glass beads	thresholding, 3D	LB simulations
Schnaar and Brusseau [2006]	SYN	10.9	sand	region grow., 3D	organic liquid dist.
Udawatta et al. [2006]	MED	190	soil	manual, 2D	macropore properties
Van Geet et al. [2003]	M-IND	22	limestone, sandstone	thresholding, 3D	porosity
Vogel et al. [2005]	M-IND	15	sintered glass	thresholding, 3D	characteristic curve
Wildenschild et al. [2002]	IND, MED, SYN	6.7–368	sand	thresholding, 3D	NA

[a]Abbreviations are as follows: IND, industrial CT; MED, medical CT; M-IND, microfocus industrial CT; SYN, synchrotron microtomography; LB, lattice-Boltzmann; NA, not applicable.

Figure 2.1 Categorization of pore-scale studies (Iassonov et al. 2009)**.**

Olivier et al. 2005 scanned a carbonate rock sample with X-ray microCT to explore the relationship between waterflooding efficiency and the rock heterogeneity. Georgiadis et al. 2013 scanned a glass bead column to explore the distribution of non-wetting phase clusters after wetting and non-wetting phase injections using an X-ray microCT scanner.

Larpudomlert et al. 2013 used the X-ray microtomography technique to scan a bead column consists of glass and plastic beads. They made a comprehensive fluid blob volume analysis at residual saturations and demonstrated that water blobs counted after non-wetting phase injection were higher than that of oil blobs at residual oil saturation because of the difference in wetting preferences of bead types. Furthermore, they

demonstrated that there is a modest difference in surface area of water and oil blobs because of the wetting strength difference between phases.

Naghavi & Kibbey 2014 performed experiments to examine the behavior of residual wetting-phase saturation according to different drainage rates using various porous media with different grain sizes. They suggested that there is a direct correlation between residual wetting-phase saturation and the rate of saturation. They also reported that deviation from this correlation is considerably affected by viscosity of the wetting fluid and is inversely proportional to the mean grain size of the medium.

Marques & Appoloni 2015 injected different fluids into a glass bead column and obtained images after X-ray microCT scanning. Then, they compared segmentation performances of these images with different concentrations of fluids injected and obtained higher segmentation performances at high KI concentrations.

Basic fluid and rock properties are not enough to characterize fluid flow in a porous medium such that fluid-fluid and fluid-rock interactions should be taken into account (Dalla et al. 2002; Culligan et al. 2004). Interfacial area have considerable effects on capillary pressure-saturation curves (Hassanizadeh & Gray 1993). Capillary pressure and saturation are not linearly dependent and they cannot be analyzed without previous knowledge of the saturation history (Chen et al. 2007).

Dalla et al. 2002 performed an artificial drainage into a water-wet synthetic porous medium using a simulator proposed by Hilpert & Miller 2001. They investigated the interfacial areas after the non-wetting phase injection into the packing and tested the success of their simulations against previous experimental and numerical works done.

They obtained the highest meniscus interfacial area at a low wetting-phase saturation as expected.

Culligan et al. 2004 proposed a study on measuring interfacial areas in a simplified porous medium composed of glass beads. They scanned the bead column using synchrotron X-ray microCT. By using high resolution microCT images, they obtained a^{wn}-S_w curves during wetting and non-wetting fluid injections. They recognized the effect of contact angle hysteresis under dynamic saturation conditions which results in highest a^{wn} values to be seen during drainage compared to imbibition (Figure 2.2a). They showed that interfacial areas between immiscible phases get its highest value in a wetting-phase saturation interval of 0.2-0.35 which confirms previous experimental findings of Dalla et al. 2002. In addition, they saw a similar trend when they used soltrol instead of air as non-wetting phase (Culligan et al. 2006) (Figure 2.2b).

a. b.

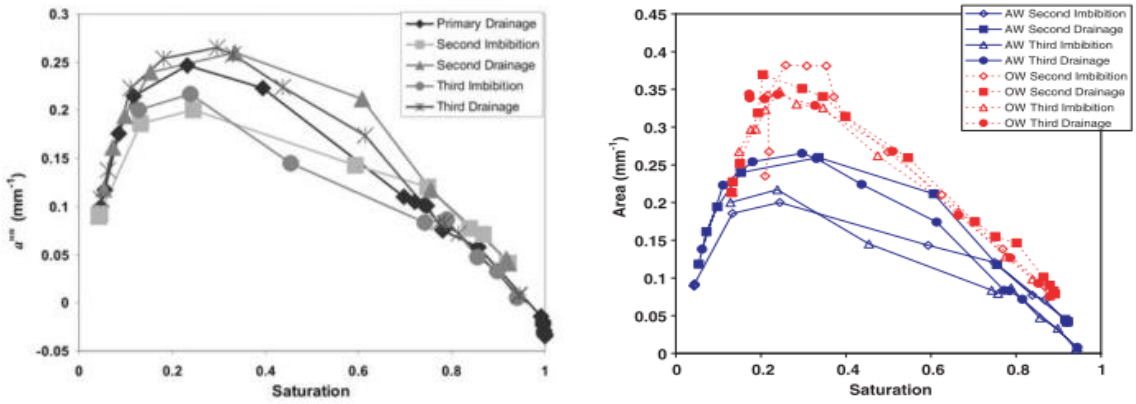

Figure 2.2 Change in meniscus interfacial area in accordance with wetting-phase saturation. a) (Culligan et al. 2004)**, b)** (Culligan et al. 2006)**.**

X-ray computed tomography is a non-destructive technique that uses X-ray beams and mathematical algorithms to visualize the interior and exterior structure of a material, thus the term computed tomography (Wellington & Vinegar 1987). By using X-ray microCT, quantitative X-ray attenuation coefficients , which are a function of density and the atomic number of the related material, are used to represent the inner structure of a sample (Iassonov et al. 2009). Pore-scale information that the numerical models need is attainable by use of X-ray microCT imaging. Although it has applications in many different fields, X-ray microCT imaging has been proven to be a powerful technique in characterizing pore-scale properties of rocks or synthetic pore structures (Culligan et al. 2006; Karpyn et al. 2007; Karpyn et al. 2010; Schlüter et al. 2010; Marques & Appoloni 2015).

In spite of all the effort that has been done, there still remains a need in generating benchmark experimental data to validate pore-scale models. As well as providing data, this study also provides a framework to better understand the effect of compaction on residual fluid distributions and interfacial areas among multiple phases using a small-scale artificial porous medium. To do so, immiscible fluid injections were performed through a water-wet synthetic glass bead packing at different axial loadings. X-ray microCT was found to be a useful technique to quantify the change in those properties. High resolution images were then used for indirect measurements of porosity, permeability, residual saturations and interfacial areas using Avizo Fire 8.0 imaging software. Generated experimental data obtained from this study could be used for validation of some pore-scale numerical flow models.

Chapter 3 : Problem Statement

Reservoir compaction caused by reservoir depletion is an important fact and it has a significant effect on hydrocarbon production (Nagel 2001; Settari 2002). It is widely known that reservoir parameters are induced by compaction. This phenomena is mostly studied at field-scale and pore-scale experimental data is needed to better understand its affects at micro-scale.

In this study, we used an artificial porous medium consists of glass beads and a specially designed core holder capable of applying radial and axial stress simultaneously. Then, by injecting immiscible fluids into the bead packing in a sequence, we investigated conventional macro-scale and micro-scale properties of surface and interfacial areas with increasing compaction. Besides, we took the advantage of X-ray microtomography which became a popular technique in these kind of pore level experiments. By doing so, we tried to provide answers to following scientific questions:

- How traditional properties of porosity, permeability and effective permeability response to changes in pore structure caused by compaction?
- What is the impact of compaction on residual fluid distributions and saturations?
- How fluid surface and interfacial areas among immiscible phases are affected by compaction?
- How sensitive are surface areas of wetting and non-wetting phase to changes in pore space and how consistent are they with linear approximations.

In order to explore those facts, we were sought to obtain vertical profiles of porosity and saturations along the bead column from three dimensional image sequences

collected. We also aimed to obtain the relationship between interfacial areas among phases and increasing axial loadings.

Chapter 4 : Methodology

Flooding experiments were performed in a glass bead packing at various axial load conditions to investigate variation of macro- and pore-scale properties in accordance with that loading. Brine and soltrol were two immiscible fluids used to represent water and oil phases, respectively. Distilled water with 6% by weight sodium iodide (NaI) was used to make a brine solution, referred to as the "wetting-phase", or "water", throughout this document. NaI was used to tag the wetting-phase, making it more distinguishable from the non-wetting and solid phase during the scanning process. The surface tension and viscosity of the brine solution are 78 mN/m and 1 cp, respectively. The specific gravity and viscosity of oil (Soltrol 170, purchased from Chevron Philips chemical company) was 0.78 (@60°F) and 2.028 cp, respectively. Soda-lime glass beads were used to create permeable columns for flow experiments. The beads have a specific gravity of 2.5 g/cm^3 and diameter ranging between 0.710 and 0.850 mm. Other physical properties of glass beads are shown on Table 4.1.

The core holder assembly allows a packing that is 1" in diameter and 2.5" in length. Glass beads were poured into the jacket at once to prevent layering of beads, which could create localized changes in mechanical and transport properties of the sample. The sample was then compacted with a metal rod by exerting load on top of the bead pack.

Table 4.1 Physical characteristics of soda lime glass beads from Mo-Sci Corp.

Bulk Density	1.3 g/cm3
Ph in water @25°C	7.8
Softening Temperature	650 °C
Thermal Conductivity	0.9-1.3 W/m.K
Coefficient of Thermal Expansion	90x10-7/°C (30-300 °C)
Compression Strenght	29 kg/mm2

4.1. Core Holder Design

A special core holder was designed and built to perform the proposed flow experiments. The core holder is a triaxial type cell, which enables simultaneous radial and axial pressure loading. Since the core holder is made of polycarbonate, it is quite suitable for X-ray CT imaging. The installation consists of a base plate, two stainless steel flow distributors, a polycarbonate vessel body, a hydraulic cylinder to apply axial stress, connection elements, bolts and spacers. Inlet and outlet flow lines from the side enter the flow distributor through an annulus with sealed o-rings as showing in Figure 4.1.

The flow distributors have tapered ends to assist the jacketing seal. Since the diameter of the flow channels in the flow distributors were larger than the average diameter of the beads, nylon screens were used to prevent the beads from passing through both channels to the flow line. A compact hydraulic cylinder, capable of 140 bar (2030 psi) loading, was used to exert axial load on the bead packs. Radial stress was controlled by confining pressure which was provided by compressed air. A 1/16” thick flexible fluoropolymer sleeve was used to isolate the packed column of glass beads from the

confining fluid. The ends of the flow distributors were lubricated with grease before assembly to give a better seal. Compressed air was used as confining fluid.

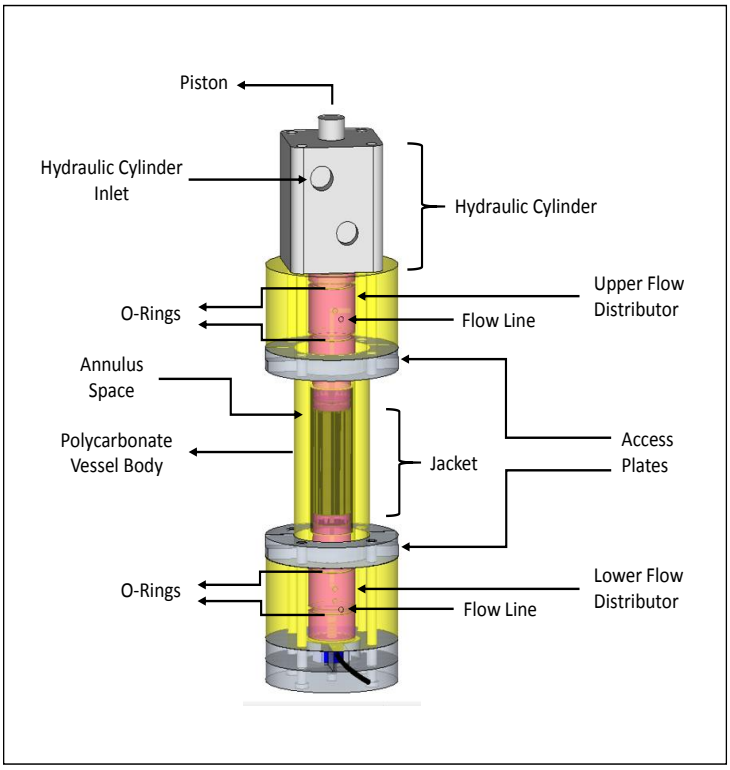

Figure 4.1 Components of core holder assembly designed by CQI laboratory staff.

4.2. Experimental Set-Up

The experimental set-up consists of a fluid reservoir, a vacuum pump, two injection pumps, a fluid overflow tank, core holder and X-ray microCT scanner (Figure 4.2). The overflow tank which has three sections was used in order to have a constant pressure head. It has a manual crank-driven system that enables a change in height of the tank while maintaining the fluid levels in the tank to obtain different pressure heads. The height difference between the second section of the tank and the outlet of the core holder provides the required pressure head to flow. Water and soltrol were mixed in the fluid

reservoir before injections in order to reduce mass transfer between phases during the displacement (Karpyn et al. 2010). Fluid was collected with a graduated cylinder at the outlet of the core holder for each pressure head value. Excess fluid was drained from the third section of the tank back into the fluid reservoir. A vacuum pump and two injection pumps were used in the experiment. Injection pumps were operated with compressed air of 70 psig. One of the injection pumps was used to transport the fluid from fluid reservoir to the tank with an adequate flow rate. By doing so, fluid levels were kept constant at the first two sections of the tank. The second pump was connected to hydraulic head to provide axial loading. Distilled water provided by the second pump was squeezed into the hydraulic cylinder to move the piston and increase axial load on the bead column to predetermined levels. Pressures and flow rates provided by the pumps were monitored and adjusted on a computer system.

A compressed air line that supplies 70 psig pressure was connected to the core holder from the side to apply confining pressure on the column of bead packs. Radial stress is limited by functional capabilities of the core holder. Since the core holder used in the experiment is made of polycarbonate and was not pressure tested, it was understood that 70 psig radial stress would be enough for rearrangement of the beads. Therefore, confining pressure was kept constant at 70 psig throughout the experiments.

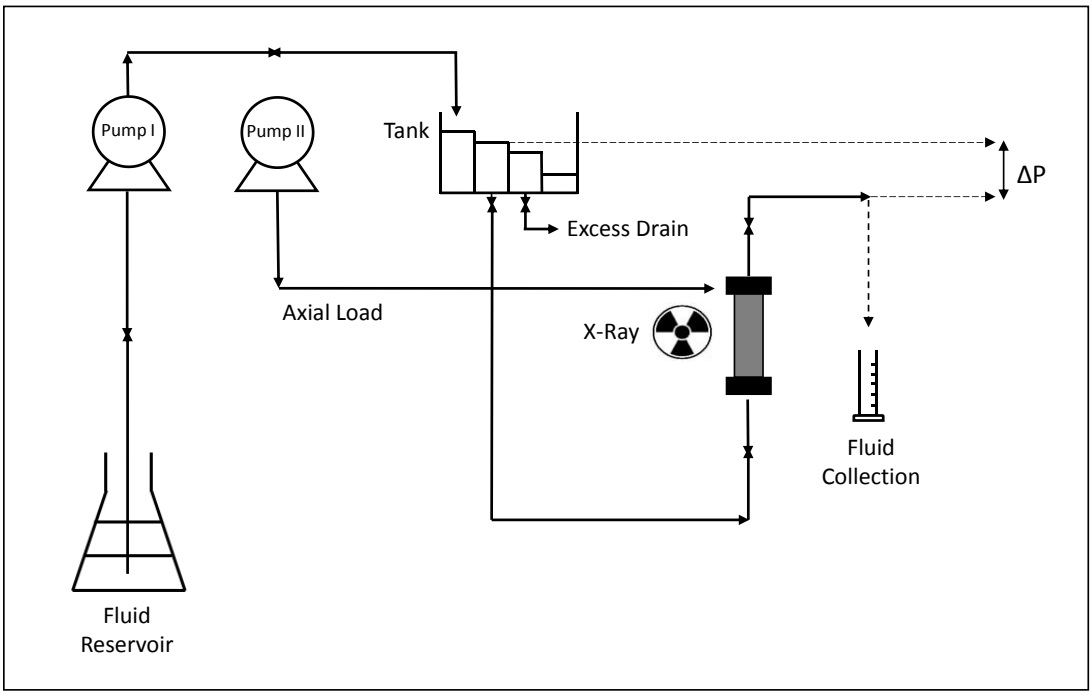

Figure 4.2 Schematic diagram of the experimental set-up.

4.3. Flooding Experiments

Before conducting the multiphase flow experiment, a single-phase flow was performed for the purpose of measuring absolute permeability at different axial loads. A bead column of 2.5” in length and 1” in diameter was prepared and pre-saturated with water. Distilled water was then injected through the bead pack from bottom to top. The pressure head was adjusted by using a pressure head maintenance tank. Flow rates were measured by monitoring the volume of fluid in the graduated cylinder at the outlet of the core holder. The flow rates were measured three times, at five different heights, and the volume averaged flow rate values were used in the absolute permeability calculations. According to Darcy’s law, flow rate and the pressure head are linearly dependent:

$$q = -\frac{kA}{\mu}\frac{\Delta P}{L}$$

Where q is the flow rate in cm^3/s, ΔP is the pressure drop in atm, L is the length of the bead column in cm, μ is the viscosity of the fluid in cp, A is the cross-sectional area open to flow in cm^2 and k is the absolute permeability in Darcy. Permeability can be found from slope of Darcy velocity (q/A) vs. ΔP graph (μ and L are already known).

Axial load on the bead packing was gradually increased and absolute permeability was measured for loadings of 50, 100, 150, 250 and 350 psig, respectively. Absolute permeability measurements at different axial loads are presented in Table 5.2 in the results chapter. After measuring absolute permeability, a new bead column was prepared under similar conditions for the subsequent multiphase flow experiment.

Figure 4.3 shows a schematic representation of the experimental procedure to examine residual phase saturations and interfacial areas at different axial loading conditions. The lighter phase (oil) was injected from the top of the sample, and the heavier phase (water) was injected from bottom to minimize gravitational redistribution of fluid phases during the injection process.

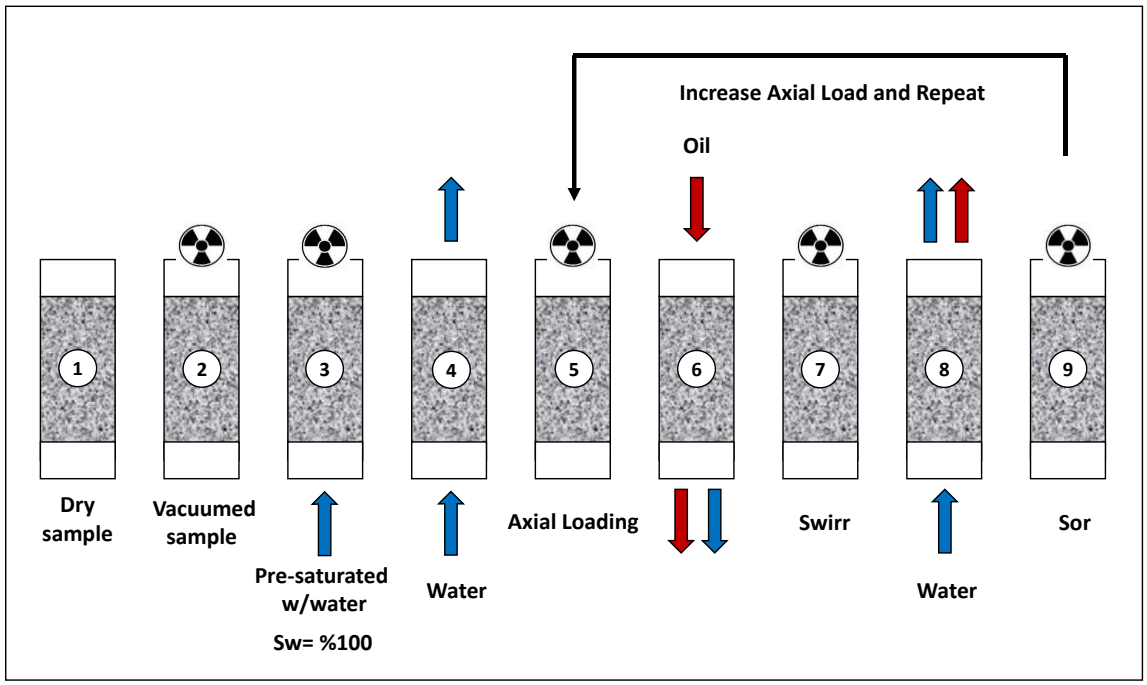

Figure 4.3 Multiphase flow experiments indicating oil and water injection steps, adapted from Karpyn et al. 2010.

Initially, the bead column was vacuumed until the vacuum pump reached approximately 89 micron and a microCT scan of dry beads was taken. A flask filled with water was placed higher than the core holder for pre-saturation. The water in the flask was heated to avoid air bubbles pass through the sample during pre-saturation. Next, the sample was pre-saturated with water from the bottom of the core and the vacuum pump was closed. Then, a microCT scan was taken at 100% water saturation.

In the fourth step, water was injected in order to measure absolute permeability which was found to be 33.5 Darcy. Absolute permeability was only measured at 0 psig, as the system was not in single-phase state after that point. In the fifth step, axial load was increased to 50 psig and the sample was scanned again. In the sixth step, 120 cc of non-wetting phase (oil) were injected from the top of the core holder at a flow rate of 0.8 cm^3/min. Following that, a microCT scan was taken at irreducible wetting-phase

saturation. In the eighth step, 115 cm^3 of wetting-phase were injected from the bottom at a flow rate of 0.6 cm^3/min. In the last step, the bead column was scanned again at residual non-wetting phase saturation. Injections were maintained until no more displaced phase was seen at the outlet of the core holder. It was seen that this was attainable by injecting approximately 4-5 pore volumes (50 to 60 cc) but more than that was injected to ensure that the system reached residual saturation conditions. Steps 6, 7, 8, and 9 were repeated at different axial load conditions of 50, 100, 150, 250 and 350 psig, respectively. In these repeated drainage and imbibition cycles, 85 to 180 cm^3 of oil and water were injected with flow rates ranging from 0.5 cm^3/min to 0.8 cm^3/min. Injection rates and amounts can be found in Table 5.4 in results chapter. While confining pressure was kept constant at 70 psig at all stages of the experiment, axial load was gradually increased up to 350 psig prior to each oil injection.

4.4. X-Ray Microtomography

In this experiment, flooding experiments were performed using X-ray microCT imaging to visualize and quantify pore space morphology under different axial load conditions. An industrial HD600 OMNI-X computed tomography scanner was used to scan the column of bead packs (Figure 4.4). This scanner provides three axes of motion: rotation, vertical, and horizontal. The rotational axis consists of a turntable on which the core holder was mounted, providing 360 degrees of rotation from which images are captured and tomography reconstructed. The vertical axis provides up to 1 meter of translation, of which, only 63.186 mm was used for scanning the sample. The horizontal

axis, also called the magnification axis, allows the sample to be best positioned, relative to the X-ray source and the detector to achieve the desired magnification and thus resolution. The core holder was mounted on top of a turn table between source and detector in a vertical position. X-ray CT scanner settings were adjusted as 180 kV and 110 mA. The scanner ran in "volume mode" which enables gathering of multiple slices during each rotation. High-resolution CT scanning was carried out with 6 rotations with a matrix pixel resolution of 1024x1024. In each scanning step, which took approximately 75 minutes, 1947 slices were collected with a voxel size of 0.0314 x 0.0314 x 0.0324 mm. In which, 0.0324 is a measure of the thickness of each slice. The bead packing was scanned totally 17 times and high resolution images were obtained to be used for quantification.

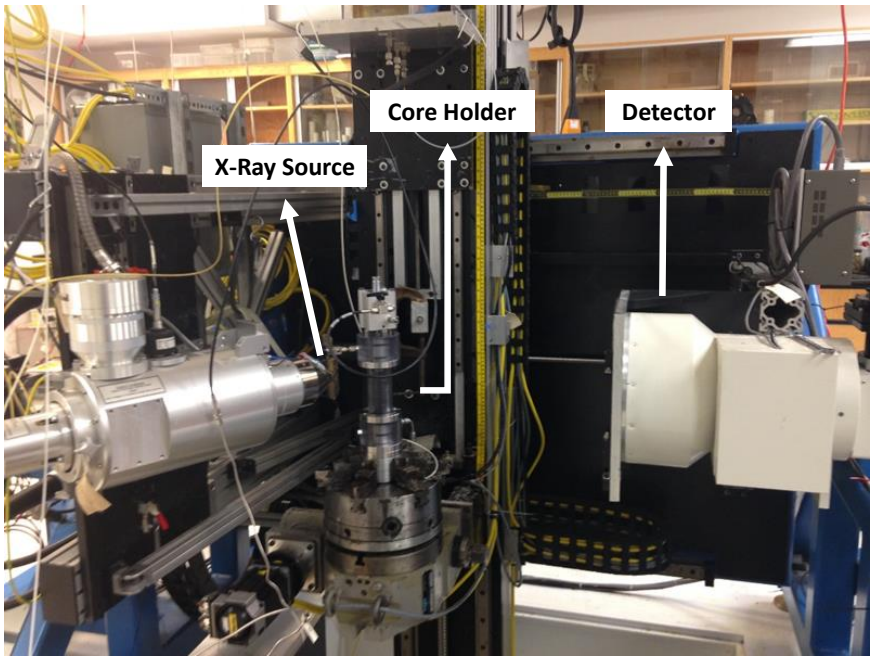

Figure 4.4 Photo of the X-ray microCT scanner and the core holder at Center for Quantitative Imaging, Pennsylvania State University.

4.5. Image Segmentation

In the last decade, X-ray microtomography has become an attractive imaging technique in order to visualize porous media (Karpyn & Piri 2007; Piri & Karpyn 2007, Karpyn et al. 2007; Iassonov et al. 2009; Schlüter et al. 2010, Wildenschild & Sheppard 2013; Blunt et al. 2013). Segmentation of generated images using X-ray microCT is the key for a successful projection of porous media (Wildenschild & Sheppard 2013).

Global thresholding is a well-known and widely used segmentation method which uses a grey-scale threshold value to distinguish two materials from each other (Iassonov et al. 2009). In this method, phases are identified based on their intensities being greater or lesser than the threshold number (Wildenschild & Sheppard 2013). Determining the threshold number is of significance by means of accuracy in the segmentation of different phases; an incorrect threshold number selected may cause deceptive results (Al-Raoush & Willson 2005; Wildenschild & Sheppard 2013). Each peak on the CT registration number-frequency histogram corresponds to a different material (Figure 4.5). The histogram pertaining to the dry beads data set in Figure 4.6 was obtained using global thresholding method in the ImageJ imaging software. A threshold number was automatically determined by the program. The CT numbers below the selected threshold represents the population of image voxels associated with the sample pore space, while the CT numbers above the threshold represents the solid glass beads. An example segmented binarized image based on that histogram is presented in Figure 4.6.

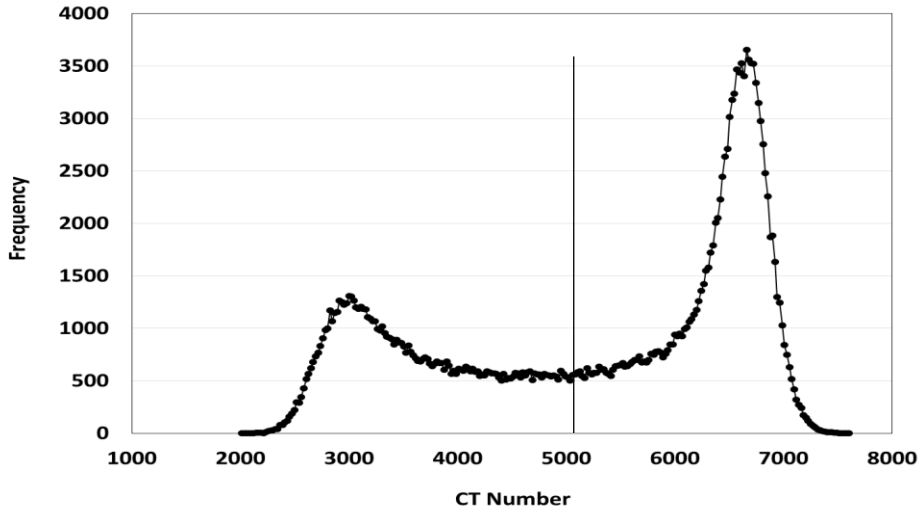

Figure 4.5 CT number histogram showing threshold value at around 5000.

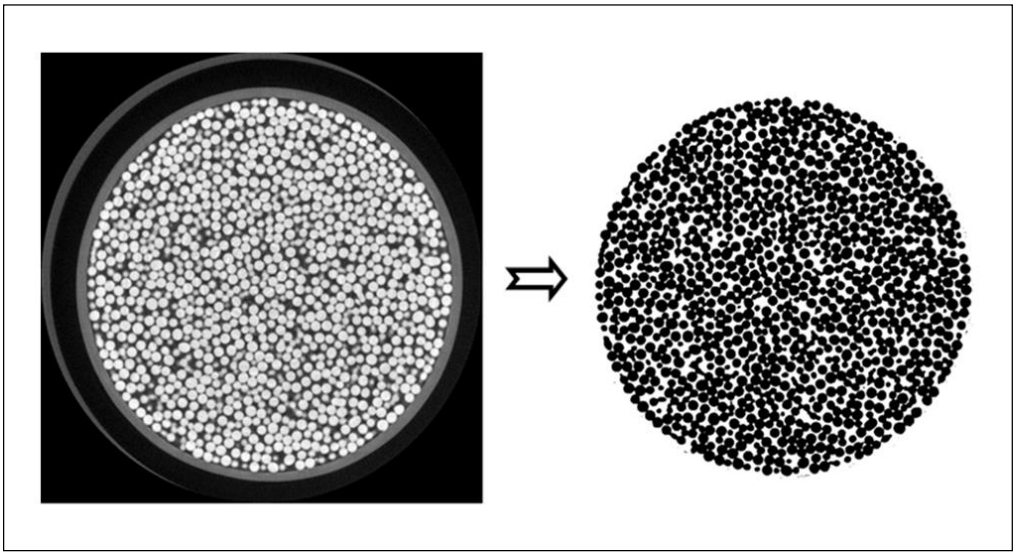

Figure 4.6 Dry beads image (left) and segmented binary image (right) by global thresholding method.

Thresholding methods are primarily useful in two-phase segmentation but they can be used to segment more than two phases by subtracting subsequent image data from the previous one after each injection (Larpudomlert et al. 2013). However, it was believed that this approach would be an impractical option for this study owing to the fact that pore structure is expected to change irreversibly as axial load increased. Therefore,

2D histogram segmentation method was adapted instead, as suggested by Torrealba 2014. In this method, different phases are assigned based on a 2D histogram of intensity and gradient magnitude of the voxels which forms CT images (Avizo Guide 2013).

The Avizo Fire 8.0 imaging software was used to quantify image data sets. After obtaining image data series of dry and pre-saturated beads, axial load was increased to the intended level and then irreducible wetting and residual non-wetting phase saturation image data sets were obtained by taking X-ray CT scans at the end of each drainage and imbibition cycle.

Image stacks corresponding each axial loading include 1947 slices. In order to neglect the impact of fluid distributors on grey-scale values, images were cropped from both ends and only 1530 slices (containing 550x550x1530 voxels) were used for analysis.

In Figure 4.7, cross-sectional views of bead packs are displayed at 50 psig axial loading.

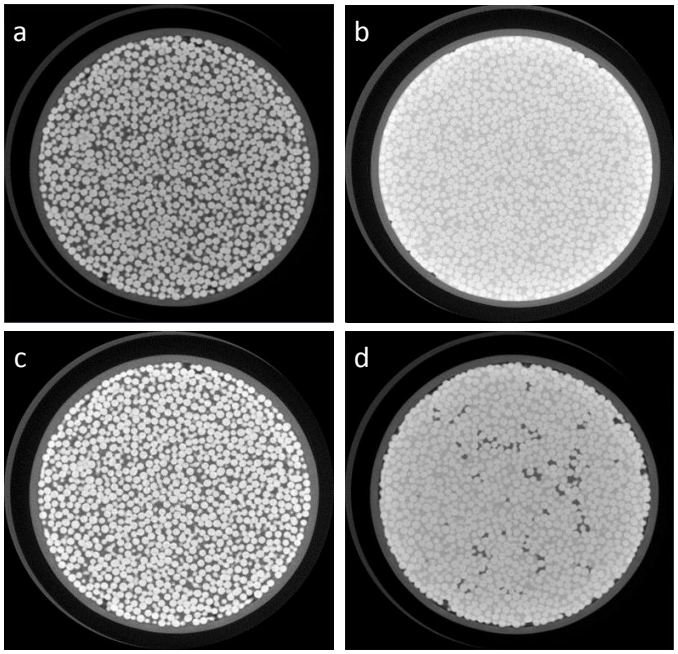

Figure 4.7 Cross-sectional views of bead packs; a) dry sample b) pre-saturated sample c) end of non-wetting phase injection (drainage) d) end of wetting-phase injection (imbibition)

In figure 4.7, the upper left image belongs to dry beads where light and the dark grey regions represent beads and pore space, respectively. The upper right image illustrates pre-saturated sample where light and dark grey regions represent beads and water, respectively. The lower left image was taken at an irreducible wetting-phase saturation whereas the lower right image was taken at a residual non-wetting phase saturation. In both lower images, the light grey region indicates glass beads and water, whereas the dark grey region indicates oil phase.

Since CT numbers of water and glass beads are close, it is a demanding task to segment them at irreducible wetting (c) and residual non-wetting phase saturations (d). A few image filtering tools were applied to images which relatively avoided artifacts and increased image quality before image partitioning. Images were cropped from top and bottom to deal with effects of flow distributors on grey-scale values and thus, on images.

After that, cropped images were filtered by several image processing tools (median filter, unsharp masking and deblur filter). These tools were applied to all images to increase contrast, sharpening and avoid blur before segmentation (Avizo Guide 2013). Example filtered images and segmented image at a residual non-wetting phase saturation are displayed in Figure 4.8. On the segmented image, the grey regions represent glass beads, blue represents the wetting-phase and red represents the non-wetting phase.

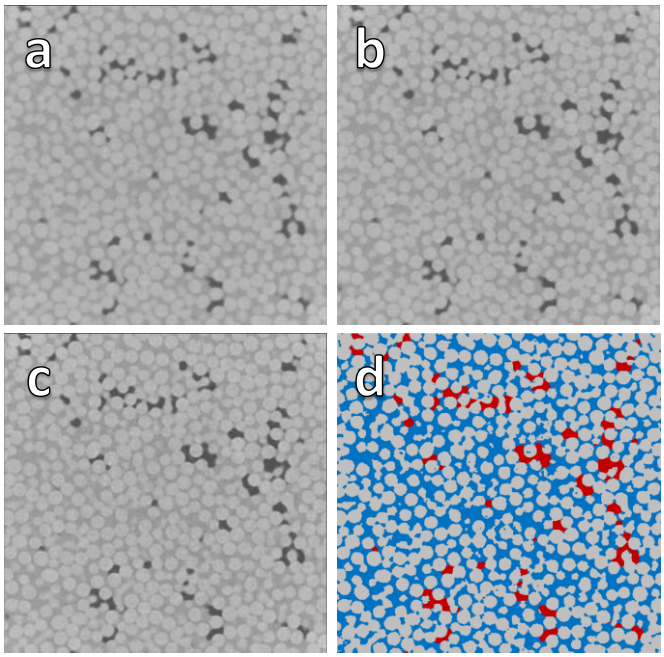

Figure 4.8 Horizontal cross-section of cropped region of interest showing filtered images and segmented image at a residual non-wetting phase saturation, 50 psig axial load. Dimensions of region of interest: 17.27x17.27x49.57 mm. Sequence: a) Median filter, b) Unsharp masking, c) Deblur filter, d) Final segmentation.

It is worth noting that, during image analysis and segmentation, the presence of air was detected within the bead column at 150 psig axial load and subsequent loadings. Therefore, air had inadvertently entered the column during the experiment and shows itself as a separate fluid phase, at saturations ranging from 6.2% to 27.2%. Figure 4.9 shows air saturation inside the column at different axial loadings. It is possible that axial loading over 100 psig may have created enough deformation of the jacketing material for

air to momentarily infiltrate from the confining space. In the analysis of fluid distribution presented in this work, the fluid phases are designated as wetting and non-wetting, where the wetting phase is water and the non-wetting phase is the sum of oil and air.

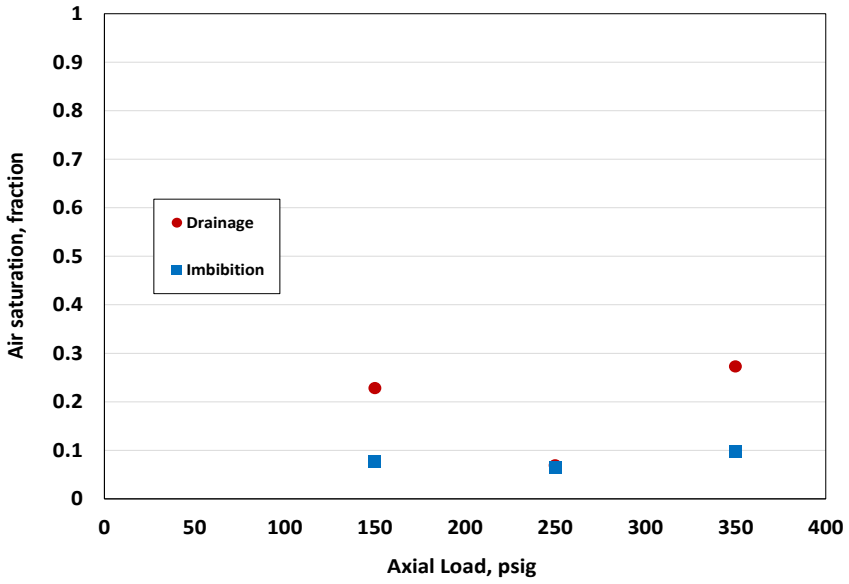

Figure 4.9 Air saturation with increasing axial load at the end of each drainage and imbibition cycle.

Chapter 5 : Results and Discussion

5.1. Porosity and Permeability

In this work, the purpose was to explore fundamental macroscale properties and interfacial areas in accordance with axial loading in a water-wet porous medium, experimentally. Therefore, a synthetic porous medium made of glass beads was built and tested under variable stress and flow conditions in laboratory setting. In this section, we present findings on porosity, absolute and relative permeability.

The Avizo Fire 8.0 image software was used to visualize and quantify variation in pore structure and fluid distribution as the axial load increased. Each of the original image data stack was composed of 1947 slices (corresponding a core length of 63.186 mm), of which, only 1530 (49.653 mm) were used for quantification to avoid imaging artifacts caused by the metal flow distributors. The cropped and segmented image sequences were used to find porosities by calculating volume fractions of each phase in each slice. The same calculations were then made for each axial load condition ranging from 50 to 350 psig. As it can be identified from Figure 5.1, increasing axial load did not translate into a significant change in porosity, even at high loadings. Although porosity is expected to decrease with increasing axial load, it could be speculated that constant radial stress (70 psig) was not sufficient to stabilize axial loadings, thus causing a slight rearrangement of beads without a significant change in net porosity. Confining pressure was kept constant at 70 psig at all stages of the experiment. Even though the confining pressure was constant, axial load was increased to 50, 100, 150, 250 and 350 psig,

respectively. In doing so, the total length of the bead column was reduced by 2.012 mm at axial load of 350 psig.

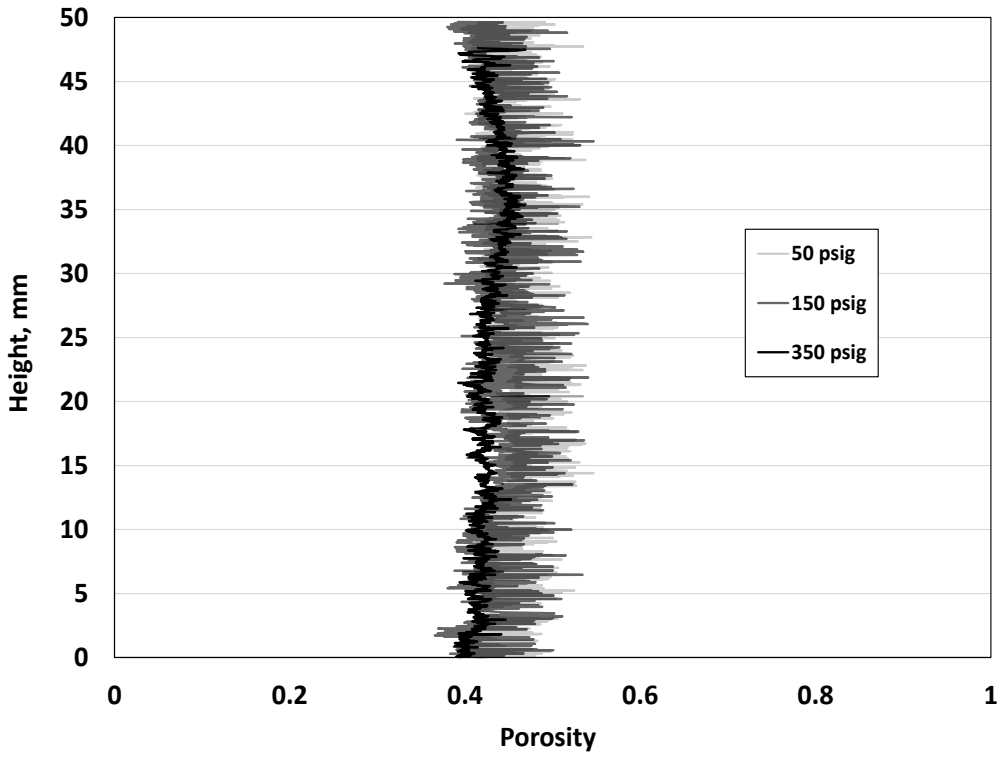

Figure 5.1 Vertical profiles of porosity at different axial loadings.

Average porosities lie within a narrow range of values from approximately 42.66% to 44.83%. The height of the bead column at 350 psig is 2.012 mm lower than others which can be considered as a proof of axial strain to some extent at that pressure. It was also noted that the standard deviation of porosity measurements by slice decreases from 3.50% to 1.49% as axial load increased. Average porosity at different axial loads are presented in Table 5.1, where porosity decreases 4.84% from 50 through 350 psig. At intermediate axial loadings, porosity remained almost the same. Lowest and highest porosity were observed at both end points of loading. The overall trend in porosity curves indicate that the packing is mostly homogeneous in majority of loadings.

Table 5.1 Average porosity values at different axial loadings.

Axial Load, psig	Average Porosity, fraction	Measurement Error
50	0.4483	0.0175
100	0.4307	0.0117
150	0.4376	0.0169
250	0.4411	0.0163
350	0.4266	0.0075

Single phase flow through the bead pack also allowed absolute permeability measurements as a function of loading conditions. A pressure head maintenance tank was filled with distilled water. The tank was placed on a crank-driven system which enables the tank to move freely up and down. Distilled water was injected from the bottom of the bead packing. Flow rates that correspond to pressure heads at specific heights were measured at every 2 minutes. Flow rates were measured three times for each pressure head in order to obtain more accurate results. Those three measurements were then averaged. Friction was taken into account and the necessary corrections were made in the calculations based on that friction.

Absolute permeability was obtained from Darcy's equation. The slope of Darcy velocity versus pressure drop is a function of permeability (k), viscosity of the fluid used (μ) and the length of porous medium (L) (Figure 5.2). In the calculations, actual velocity was used which is the ratio of apparent Darcy velocity to porosity.

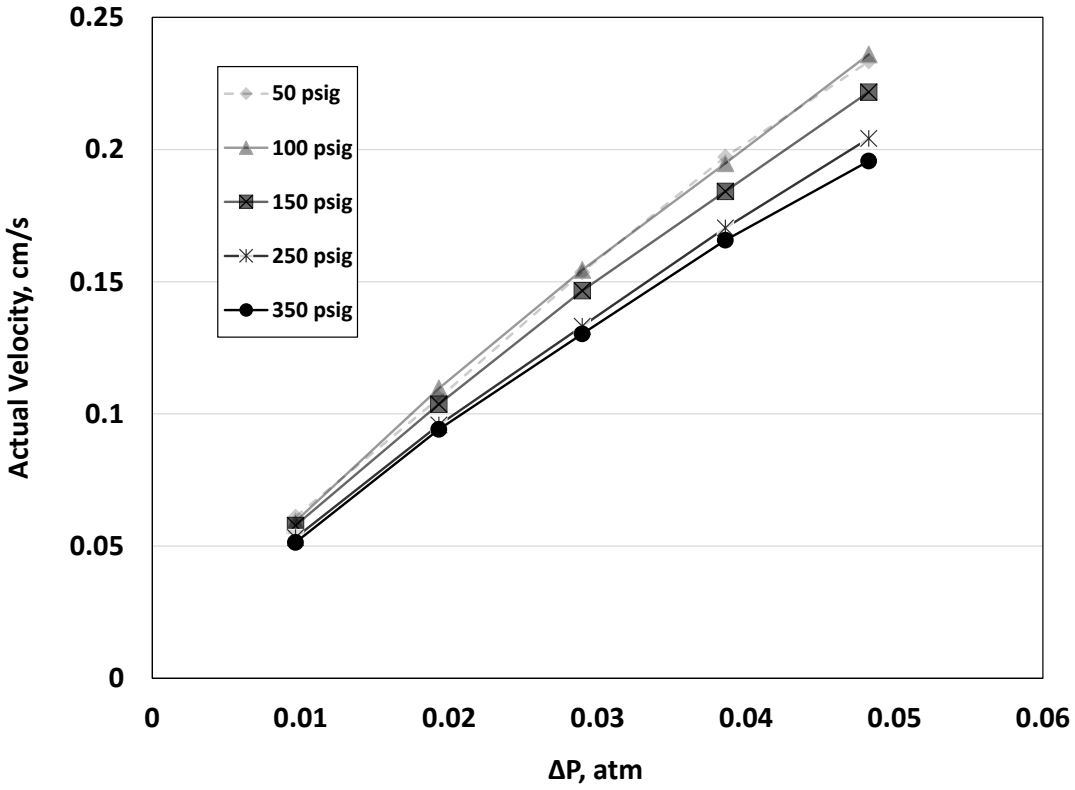

Figure 5.2 Actual velocity curves at different axial load conditions.

There is a comparable decline in absolute permeability as axial load increased. However, it slightly increased in between 50 and 100 psig. An absolute permeability of 31.63 Darcy was found without any axial loading. Figure 5.3 shows absolute permeability values according to axial loadings. Absolute permeability dropped from its initial high value of 30.39 to 25.11 Darcy. The percentage of decrease in absolute permeability from 0 to 350 psig axial load are presented in Table 5.2. The largest decrease in permeability drop occurred in between 150 and 250 psig (7.83%).

Table 5.2 Absolute permeability changes with axial loading.

Axial Load, psig	Absolute Permeability, Darcy	Permeability Drop, %	Measurement Error
50	30.39		0.0715
100	30.57	-0.57	0.0759
150	28.47	6.85	0.0554
250	26.25	7.83	0.0111
350	25.11	4.31	0.1026

We observed a slight decrease in absolute permeability and there is also a slight decrease in porosity that justifies the change in permeability. Average porosity and absolute permeability are illustrated simultaneously in accordance with axial loading in Figure 5.3.

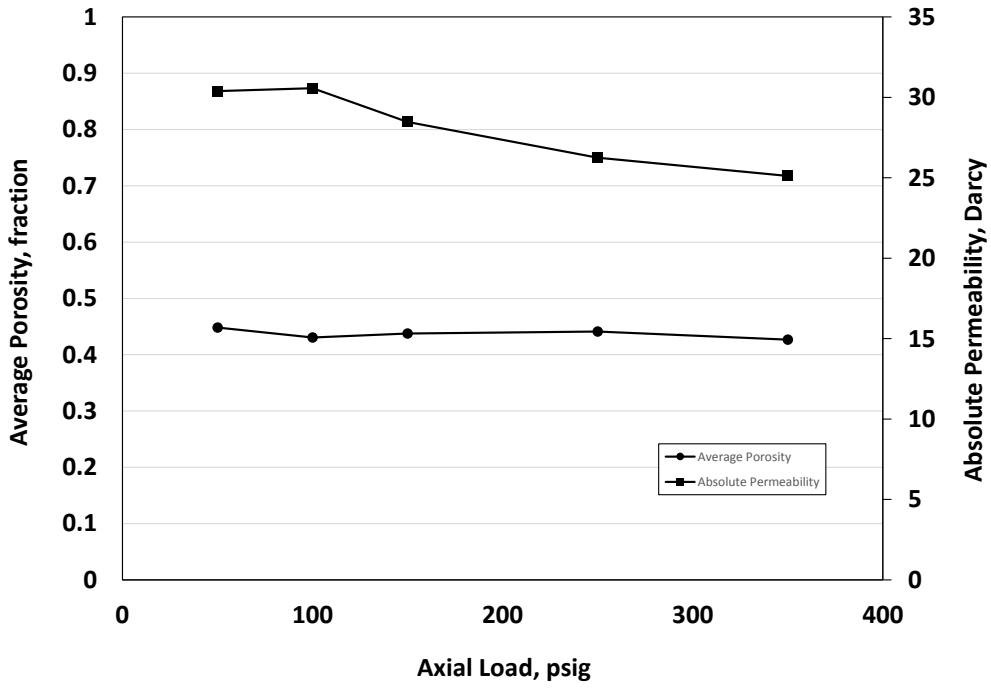

Figure 5.3 Average porosity and absolute permeability at different axial load conditions.

In Figure 5.3, we are able to compare how porosity and absolute permeability are changing with different axial loadings. We see that average porosity remains nearly constant which is consistent with what we saw in the previous vertical porosity profiles in

Figure 5.1. There is a minor decrease in porosity but on the whole, it is fairly constant. In case of absolute permeability, we see a decrease which goes from 30.39 to 25.11 Darcy. The absolute permeability drop can be considered to be a minor decrease for the type of experiments that we are performing.

As it was mentioned earlier, axial loadings that we applied did not considerably translate into compaction. It is evident from the results that axial loading induced rearrangement of the beads without a significant change in pore structure. It could also be linked to lack of confining pressure applied which was not sufficient to compensate axial loadings over 70 psig.

5.2. Relative Permeability

Effective permeability is a measure of how easily a fluid flow in the presence of other immiscible fluids within porous medium and it has great significance in reservoir engineering (Osoba et al. 1951). In addition to absolute permeability, effective permeability to oil and water were measured individually at different axial load conditions. Effective permeability was measured at both residual wetting and non-wetting phase saturations. Oil was injected from the top of the core and after the irreducible wetting-phase saturation was reached, oil continued to be injected at different pressure heads to measure effective permeability to oil. Water was injected from the bottom until residual non-wetting phase saturation reached and the same procedure was followed to measure effective permeability to water. End point relative permeability (k_{rw} and k_{ro}) values were found by dividing effective permeability to absolute permeability for each

axial loading. A modified form of Brooks and Corey (MBC) model was used to obtain relative permeability curves from end point relative permeability values (Alpak et al. 1999).

$$k_{r1} = k_{r1}^{\circ} \left(\frac{S_1 - S_{1r}}{1 - S_{1r} - S_{2r}}\right)^{n_1}$$

$$k_{r2} = k_{r2}^{\circ} \left(\frac{1 - S_1 - S_{2r}}{1 - S_{1r} - S_{2r}}\right)^{n_2}$$

where:

k_{r1}, k_{r2} : End point relative permeability of wetting and non-wetting phase.

S_{1r}, S_{2r} : Residual wetting and non-wetting phase saturations.

n_1, n_2 : Exponents to be fit to experimental data.

Table 5.3 shows end point relative permeability values at residual saturation states. Relative permeability curves obtained from above equations can be found in Figure 5.4.

Table 5.3 End point relative permeability to wetting and non-wetting phase at residual saturation conditions.

Axial Load, psig	kro, Swirr	krw, Sor
50	0.4236	0.5623
100	0.0252	0.2072
150	0.3109	0.2628
250	0.1912	0.4007
350	0.1032	0.1782

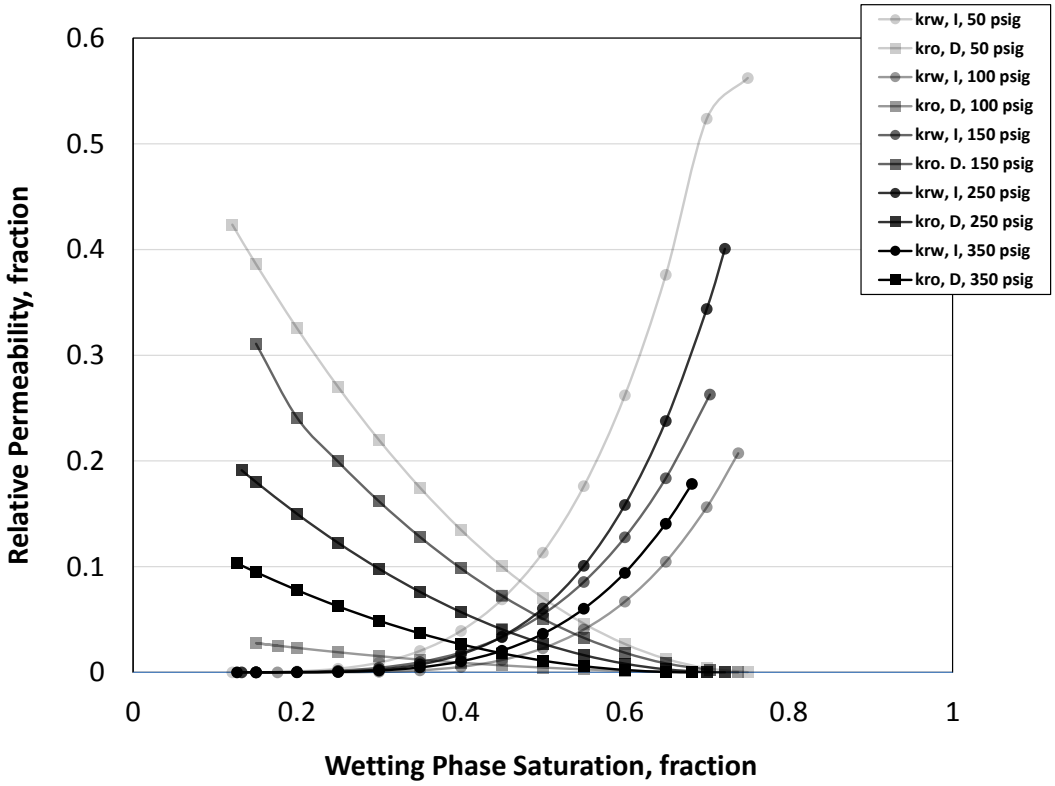

Figure 5.4 Relative permeability curves at different axial load conditions. The shaded-in color was darkened for both symbols and lines as axial load increased. I and D represents imbibition and drainage, respectively.

These curves in general become more depressed as axial load increased and residual saturations are similar for most of these drainage and imbibition curves.

5.3. Residual Saturations

Referring back to the methodology section, after the bead packing was vacuumed, it was pre-saturated with water (wetting-phase). Oil (non-wetting phase) was then injected from the top of the core to displace all mobile water until the system reached irreducible water saturation (drainage). Oil injection was stopped when the displaced phase was no longer produced at the outlet of the core. Water was injected from the

bottom of the core following each drainage step, until residual oil saturation was reached (end of imbibition). Similarly, water injection was stopped when the displaced phase was no longer produced at the outlet of the core. During drainage and imbibition cycles, approximately 7-9 pore volumes were injected with flow rates ranging from 0.5 to 0.8 cm^3/min. Injections were repeated at different axial loads to investigate the impact of loading on fluid distributions. At the end of each fluid injection, a microCT scan of the sample was taken to map fluid distribution. Injection data are presented in Table 5.4.

Table 5.4 Injection rates and amounts during each drainage and imbibition cycle at different axial loadings.

Axial Load	Injected Fluid	Cycle	Injection Rate, cc/min	Pore Volume Injected	Water Saturation, fraction
50 psig	Soltrol	Drainage	0.8	8.48	0.1210
	Brine	Imbibition	0.6	8.13	0.7613
100 psig	Soltrol	Drainage	0.5	12.72	0.1762
	Brine	Imbibition	0.5	7.07	0.7384
150 psig	Soltrol	Drainage	0.7	7.07	0.0747
	Brine	Imbibition	0.8	7.07	0.7039
250 psig	Soltrol	Drainage	0.6	6.01	0.1324
	Brine	Imbibition	0.6	7.07	0.7221
350 psig	Soltrol	Drainage	0.5	7.07	0.1267
	Brine	Imbibition	0.6	7.77	0.6819

Segmented image sequences belonging to drainage and imbibition were used to compute residual fluid saturations, with the assistance of the Avizo Fire 8.0 software. To do so, volume fractions of each phase in each slice were calculated. Next, wetting-phase (water) saturations were calculated for each slice and wetting-phase saturation distributions along the height of bead packing were then obtained. An average residual wetting-phase saturation (average of them at all axial load conditions) was calculated to be 12.62% at the end of drainage. Larpudomlert et al. 2013 reported a slightly higher wetting-phase saturation of 14.08% in a mixed wet bead column (containing glass and plastic beads) after drainage. A lower irreducible water saturation is expected in a mixed

wet media because glass beads have a stronger tendency to cohere water phase than that of plastic beads (Larpudomlert et al. 2013). This is not parallel with findings in present study. That difference might be attributed to different flow rates used. Also, in this study, variable axial loadings applied on the bead packs which also has an impact on residual saturations.

Landry 2010 reported a wetting-phase saturation of 68.37% in a glass bead packing after non-wetting phase injection (drainage). This resulting saturation is not in parallel with this study. Excessively higher residual water saturation (68.37%) could be related to the difference in displacement efficiencies between two studies. Furthermore, Landry 2010 linked this unexpected recovery to gravitational segregation which resulted in a different drainage curve in terms of homogeneity compared to Figure 5.5.

In Figure 5.5, residual wetting-phase saturations along the bead column are presented at the end of drainage, at different axial loads. Results suggest that wetting-phase saturation does not have a strong response to the increasing axial loads applied. In most of the cases, similar residual wetting-phase saturations were observed although there was a sharp decrease at 150 psig. The average residual wetting-phase saturations are ranging from 7.47% to 17.62%. The separation between curves is more noticeable at the bottom 10 mm portion of the core. The most successful displacement was achieved at 150 psig with an irreducible water saturation of 7.47%. As oil was injected from the top, lower water saturation is expected at the top of the core due to its proximity to the inlet phase. The height of the sample dropped from its original value (49.653 mm) to 47.641 mm at 350 psig which refers to axial strain of some degree.

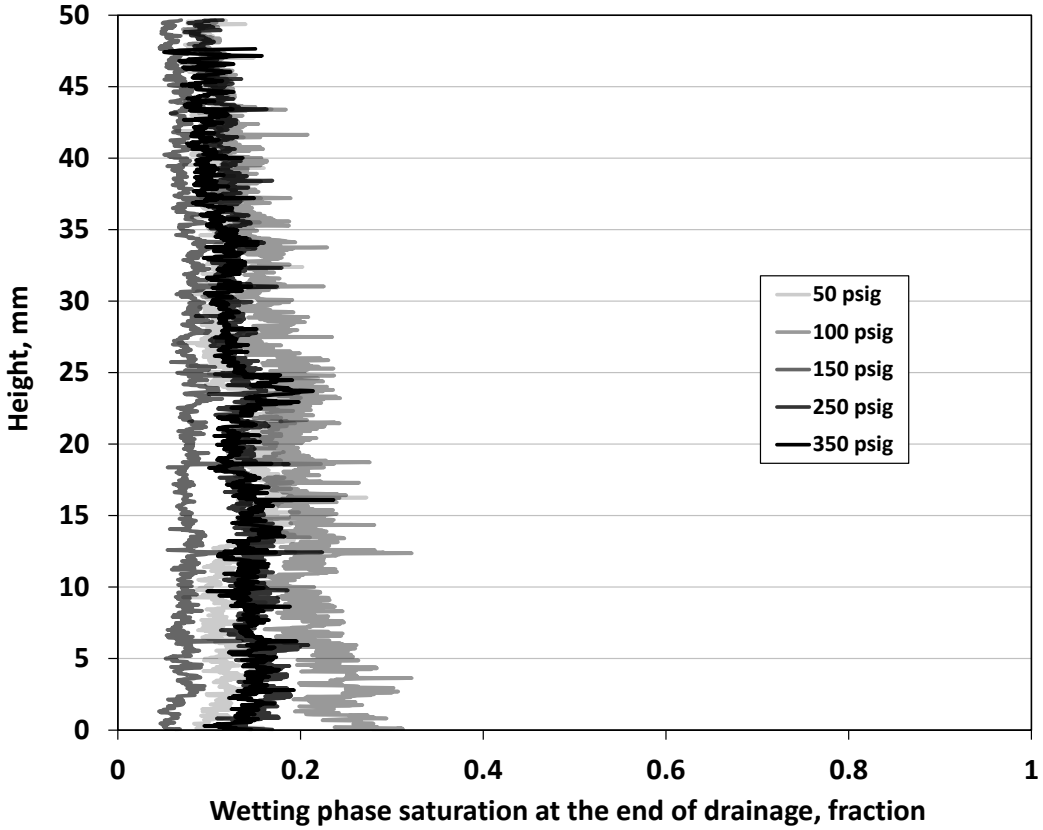

Figure 5.5 Vertical profiles of wetting-phase saturations at the end of drainage at different axial loads.

Wetting-phase saturations were again calculated per slice at the end of each imbibition cycle. Thus, vertical wetting-phase saturation profiles were then obtained along the bead packing at different axial loadings (Figure 5.6).

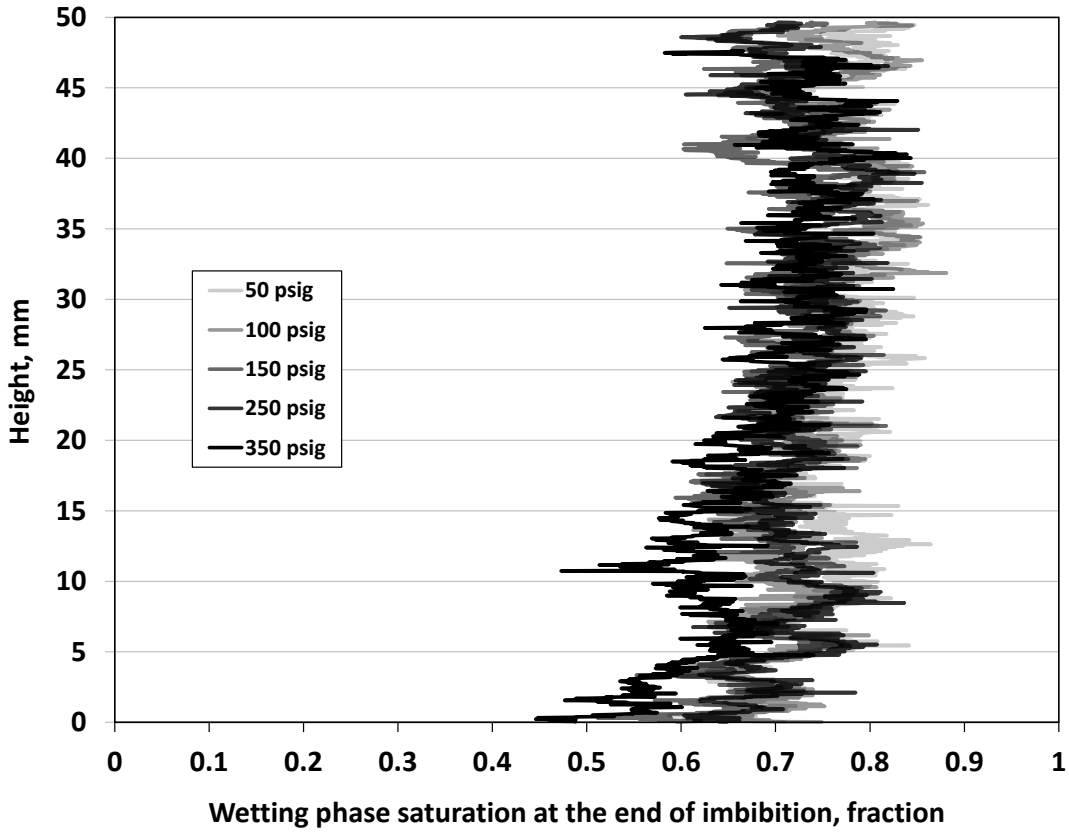

Figure 5.6 Vertical profiles of wetting-phase saturations at the end of imbibition at different axial loadings.

In order to carry out imbibition, water was injected from the bottom of the core. As it can be seen from Figure 5.6, wetting-phase saturations at the end of imbibition cycles do not seem to show a strong correlation with axial loading. It was expected to find higher wetting-phase saturations at the bottom of the core because water flooding was conducted from bottom to top. However, it is evident that wetting-phase saturations are slightly lower at the bottom. This is attributed to the presence of air mostly trapped at the bottom of the core. As stated before, air was treated as the non-wetting phase together with oil and that is responsible for slightly lower wetting-phase saturations at the bottom of the core.

We also observed that imbibition wetting-phase saturation curves fluctuate more than those of drainage. This is attributed to fluctuations could be a mixture of data noise related to CT numbers and packing variations is that the saturations were calculated per slice and slice thickness was overwhelmingly smaller than average bead diameter. In addition, due to the fact that cropped images (both from top and bottom) were used for quantification, we did not see the sign of end effects on both drainage and imbibition curves. The effect of axial strain again can be noticed at 350 psig that the length of the curve is slightly shorter than others.

5.4. Pore-Scale Interfacial Areas

In order to calculate surface and interfacial areas, the “generate surface” tool was used in the Avizo Fire 8.0 software. With this tool, a triangulated approximation of surfaces between phases is created, which allows the rendering of smoother, and therefore more accurate surfaces (Avizo Guide 2013). This triangular approximation minimizes staircase-like surfaces which cause deviations in surface area calculations (Culligan et al. 2004). Avizo uses the marching cube algorithm developed by Hege et al. 1997 to calculate surface areas. In this study, fluid and solid surface areas and total and meniscus interfacial areas between phases were studied. The meniscus interfacial area occurs between wetting and non-wetting interface (Figure 5.7).

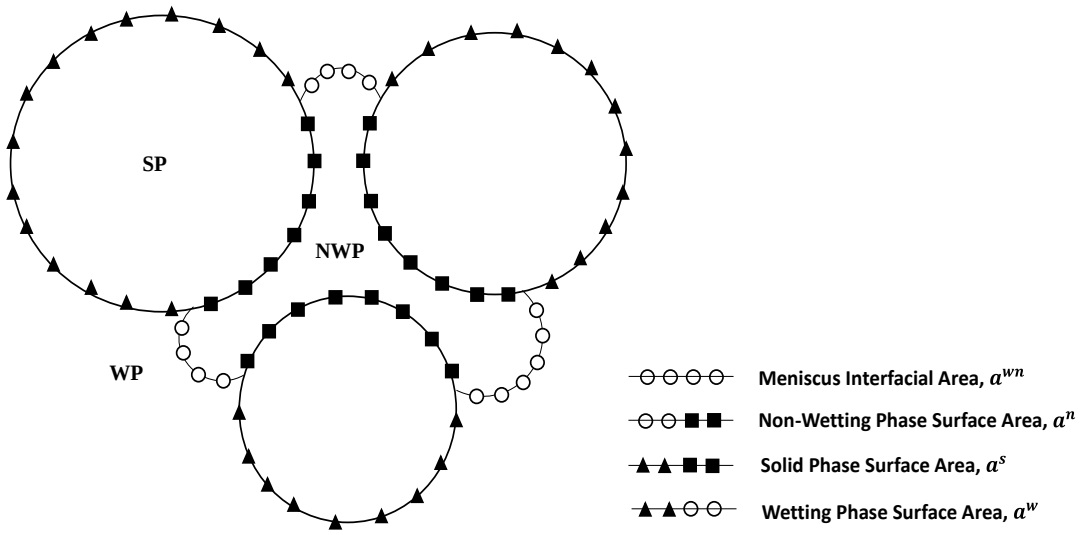

Figure 5.7 Schematic drawing of surface areas and meniscus interfacial area adapted from Dalla et al. 2002, where SP, WP and NWP are solid phase, wetting-phase and non-wetting phase, respectively.

Dalla et al. 2002 proposed an equation to calculate wetting-non wetting (meniscus) interfacial area:

$$a^{wn} = \frac{1}{2}(a^{n} - a^{s} + a^{w})$$

where, a^{n} is the non-wetting phase surface area, a^{s} is the solid phase surface area, a^{w} is surface area of the wetting-phase and a^{wn} is the interfacial area between wetting and non-wetting phase (meniscus) (Figure 5.7).

Surface area and volume of each individual phase (wetting, non-wetting and solid phase) were calculated from three dimensional image stacks (containing 550x550x1530 voxels corresponding a volume of 14851.95 mm^3). These calculations were repeated for each segmented image sequence at different axial load conditions of 50, 100, 150, 250 and 350 psig, respectively. Total interfacial areas were calculated by assuming a thin wetting film surrounding solid surfaces. Therefore, the total interfacial area, in this case correspond with the non-wetting phase surface area (Landry et al. 2011). Specific surface

areas and specific meniscus interfacial areas were computed by normalizing surface areas by bulk volume (V_b) which is the total volume of all phases present in the interested region of the sample. Additionally, wetted fraction of solid surface by the wetting and the non-wetting phases were calculated (Culligan et al. 2006). The calculations were done based on equations presented by Dalla et al. 2002, Culligan et al. 2006 and Landry et al. 2011.

Where;

Specific wetting-phase surface area:

$$a^w = \frac{Wetting\ phase\ surface\ area}{V_b}$$

Specific non-wetting phase surface area:

$$a^n = \frac{Non-wetting\ phase\ surface\ area}{V_b}$$

Specific pore space surface area:

$$a^p = \frac{Pore\ space\ surface\ area}{Pore\ space\ volume}$$

Specific solid phase surface area (glass beads):

$$a^s = \frac{Solid\ phase\ surface\ area}{V_b}$$

Specific meniscus interfacial areas (a^{wn}) and fraction of solid surface area contacting with the wetting (X_w) and the non-wetting phase (X_{nw}) were also computed by assuming that wetting-phase is not forming a film all around the solid phase (Culligan et al. 2006; Landry et al. 2011).

Specific meniscus interfacial area:

$$a^{wn} = \frac{1}{2} * \left(\frac{Wetting\ phase\ surface\ area}{V_b} + \frac{Non - wetting\ phase\ surface\ area}{V_b} - \frac{Solid\ phase\ surface\ area}{V_b}\right)$$

Fraction of solid surface area contacting with the wetting-phase;

$$X_w = \frac{a^w - a^{wn}}{a^s}$$

Fraction of solid surface area contacting with the non-wetting phase;

$$X_n = \frac{a^n - a^{wn}}{a^s}$$

Using the equations above, wetting-phase, non-wetting phase, solid, pore space specific surface areas, specific meniscus interfacial areas and wetted fractions of solid surface by the wetting and the non-wetting phase were calculated at the end of each drainage and imbibition cycle. Calculations were repeated at different axial load conditions. Findings are summarized in Table 5.5 and 5.6, respectively.

Table 5.5 Specific surface area and specific meniscus interfacial area measurements after each non-wetting phase injection at different axial load conditions

Injection Sequence	a^s, mm^{-1}	a^p, mm^{-1}	a^w, mm^{-1}	a^n, mm^{-1}	a^{wn}, mm^{-1}	S_w, fraction	X_w, fraction	X_n, fraction
50psi, Drainage	3.787	10.509	0.412	3.491	0.058	0.1210	0.0935	0.9065
100psi, Drainage	3.785	10.392	0.902	3.179	0.148	0.1762	0.1993	0.8007
150psi, Drainage	3.694	10.610	0.226	3.679	0.106	0.0747	0.0327	0.9673
250psi, Drainage	3.769	10.665	0.558	3.458	0.124	0.1324	0.1153	0.8847
350psi, Drainage	3.752	9.558	0.722	3.592	0.281	0.1296	0.1175	0.8825

Table 5.6 Specific surface area and specific meniscus interfacial area measurements after each wetting-phase injection at different axial load conditions

Injection Sequence	a^s, mm^{-1}	a^p, mm^{-1}	a^w, mm^{-1}	a^n, mm^{-1}	a^{wn}, mm^{-1}	S_w, fraction	X_w, fraction	X_n, fraction
50psi, Imbibition	3.648	11.980	3.236	0.465	0.026	0.7613	0.8798	0.1202
100psi, Imbibition	3.796	11.229	3.391	0.563	0.079	0.7384	0.8726	0.1274
150psi, Imbibition	3.524	11.414	3.023	0.636	0.067	0.7039	0.8388	0.1612
250psi, Imbibition	3.676	11.197	3.194	0.623	0.071	0.7221	0.8498	0.1502
350psi, Imbibition	3.262	10.659	2.765	0.633	0.068	0.6822	0.8268	0.1732

In a stable system, solid specific surface area (a^s) is expected to be constant. The variations in a^s values here, could be attributed to the change in pore structure due to axial and confining pressures applied on the sample. Moreover, some local lateral enlargements on the bead packing were observed with increasing axial loading which could possibly contribute to those variations. Figure 5.8 shows specific meniscus interfacial areas at residual saturation conditions.

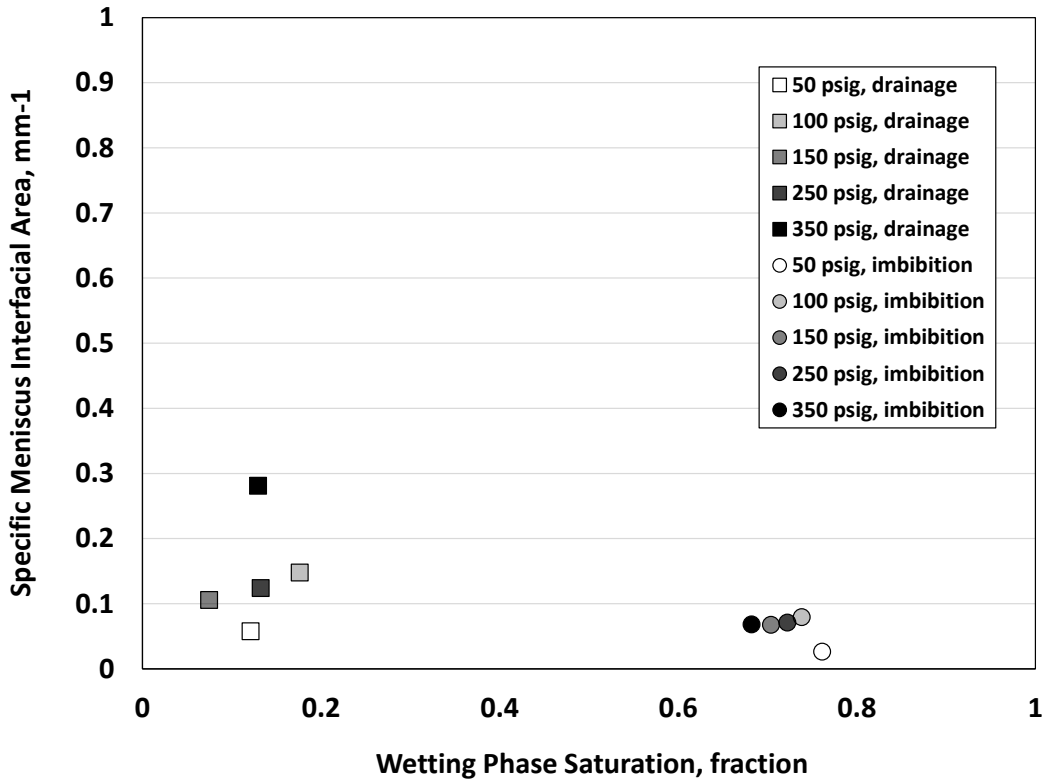

Figure 5.8 Specific meniscus interfacial areas at the end of drainage and imbibition cycles at different axial loads.

There is an observable spread in the specific meniscus interfacial area values at irreducible wetting-phase saturations based on axial loads applied (squares in Figure 5.8). The spread is appreciably wider than the one seen at the residual non-wetting phase saturations (circles in Figure 5.8). This seems to indicate more loading sensitivity in meniscus interfacial areas at the irreducible wetting-phase saturations. Although pore structures are fairly similar under the same axial load conditions, more clustered accumulation of data points were observed at the end of imbibition. Despite the fact that there is not a regular tendency in accordance with axial load in both cases, lowest specific meniscus interfacial areas were found at lowest axial load for both cases (end of drainage and imbibition). Moreover, for the wetting-phase, the lowest axial load (50 psig) leads to

the lowest specific meniscus interfacial area and the highest axial load (350 psig) leads to the highest specific meniscus interfacial area. An evident relationship was not seen for intermediate axial load conditions in both residual saturations. It can be inferred that minor changes in the configuration of solid (beads) impact the relationship of interfacial areas at irreducible wetting-phase saturations.

Higher meniscus interfacial area implies more fluid-fluid contacts between phases. The wetting-phase has a tendency to maximize its contact with the solid due to its wetting affinity. Since glass beads used in the experiment show water-wet characteristics, it is expected that water (wetting-phase) would exhibit larger contact surface area with the glass beads.

Specific surface area of the trapped wetting-phase (a^w) is higher than the non-wetting (a^n) at axial loadings of 100 and 350 psig and they are close to each other at 50 and 250 psig loadings. However, there is an exception at 150 psig and that is proven to be an exception in terms of other observations (Table 5.5 and 5.6). In general, different residual wetting and non-wetting phase saturations were found for each axial load condition. Even though residual water saturations are tend to be always lower, specific surface area of the wetting-phase is either similar or higher than that of the non-wetting with the exception of 150 psig loading. That exception could be attributed to arrival of air into the sample which might be responsible for altering some of the specific surface area results.

We obtained closest residual saturations at 100 psig axial loading for drainage and imbibition cases (Swirr= 0.1762 and Sw= 0.7384 (Sor= 0.2616)). At these saturations, the wetted fraction of solid surface by the wetting-phase at the end of drainage is 19.93%

while it is 12.74% by the non-wetting phase at the end of imbibition (Table 5.5, 5.6). As it is expected, even though wetting-phase saturation is slightly lower at the end of drainage (17.62% < 26.16%), wetted fraction of solid surface by the wetting-phase is still higher than that of non-wetting. Nevertheless, in most of the cases, we see that meniscus interfacial area is higher at the end of drainage than that of imbibition. This behavior could be linked to the tendency of wetting-phase to maximize its surface area in contact with the solid which results in a much more intricate pattern than the non-wetting phase forms. Since wetting-phase generates much more complex structures at roughly same saturations, it could potentially produces more fluid-fluid contacts than the non-wetting phase does and that might cause meniscus interfacial areas to be higher at the end of drainage cycles.

It could be concluded that the meniscus interfacial area is not sufficient to determine wettability. Furthermore, topology of the wetting and non-wetting fluid blobs are also a measure of wettability and might have an impact on interfacial areas to the point that at least at residual saturations. Although the wettability is the strongest cause on interfacial areas, it also has different manifestations. The wetting affinity that the solid phase (glass beads) has, determines the distribution of residual phases. The wetting-phase fluid blobs stretch further into multiple pores which may lead to more ends accounting for additional meniscus interfacial area. In addition, the shape of these blobs is a function of pore structure because these blob shapes adapt themselves with respect to the pore structure. A small change in axial strain could be enough to generate more crevices and more narrow pores which may assist to form a suitable medium for wetting-phase to

reside, even though it does not add up to remarkable changes in macroscopic properties like porosity and permeability.

Specific meniscus interfacial areas were found to be higher at irreducible wetting-phase saturation than the non-wetting phase saturation, which is consistent with what has been seen in previous experiments by Culligan et al. 2004. They studied fluid-fluid interfacial areas in a water-wet synthetic porous medium using microCT and they examined meniscus interfacial areas in dynamic conditions. In their case, they explained this behavior by the idea of contact angle hysteresis. This idea proposes a stretched meniscus interfacial area during imbibition relative to drainage (Culligan et al. 2004) (Figure 5.9).

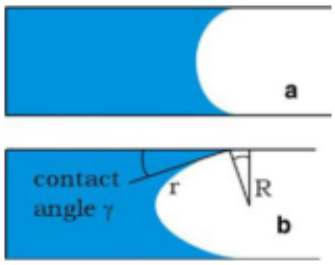

Figure 5.9 In a capillary tube, wetting-non-wetting interface is more dilated during drainage (b) than imbibition (a) (Culligan et al. 2006)**.**

However, meniscus interfacial areas were reported at equilibrium conditions in the present study and similarly, higher meniscus interfacial areas were observed at the end of drainage than that of imbibition.

What generates a larger or smaller surface area is the fact that contact angle hysteresis generates different pathways. It can be said that contact angle hysteresis would generate different pathways that these fluids penetrate and that history or the path is what generates the final different states in meniscus interfacial area. The path that those

immiscible fluids follow could cause an irreversible effect on how the final saturations are going to be distributed. The existence of the effect of contact angle hysteresis during displacement could still be responsible for the difference in meniscus interfacial areas at residual saturation states (under final static conditions). Because the stretching of those interfaces generate conditions for pore-scale displacements that at the end lead to different meniscus interfacial areas.

As it was stated before, structural distribution of phases, which is controlled by the wetting affinity of glass beads, also should be taken into account. At the end of drainage, wetting-phase occupies narrowest pores and therefore leading to more complicated structures that unavoidably results in more fluid-fluid contact areas.

Experimental results reported in the literature show the highest meniscus interfacial areas in a range of wetting-phase saturations of 0.25 to 0.55 (Culligan et al. 2004; K. a. Culligan et al. 2006; Landry et al. 2011) which differ from results obtained in this study. It could be attributed to the difference in experimental methodology followed or evaluating experimental data in a different way. Culligan et al. 2006 scanned the glass bead packing in dynamic conditions (during drainage and imbibition cycles). In this study, the bead column was scanned at static conditions (at the end of drainage and imbibition sequences) and measured wetting-phase saturations by slice were averaged. Landry et al. 2011 used different subsamples correspond to various saturations on drainage and imbibition curves along the bead packing. Also, their irreducible wetting-phase saturation (drainage) curves show much more variation than the results reported here. In this study, entire core length was evaluated at once and drainage and imbibition curves did not seem to show much hysteresis. On the other hand, meniscus interfacial

areas are so driven by the structure, in the case of small changes in bead grain distribution, variations were observed in specific meniscus interfacial areas at the end of drainage, which is not reflected at the end of imbibition.

Specific total interfacial areas were also calculated in the presence of the wetting films. Therefore, the total interfacial area, in this case correspond with the non-wetting phase surface area (Landry et al. 2011). As it can be seen from Figure 5.10 that specific total interfacial areas are not following an ordered path as axial load increased. They are greater at irreducible wetting phase saturation as it was predicted. At the end of imbibition, data points lie in a narrower bandwidth of specific total interfacial area.

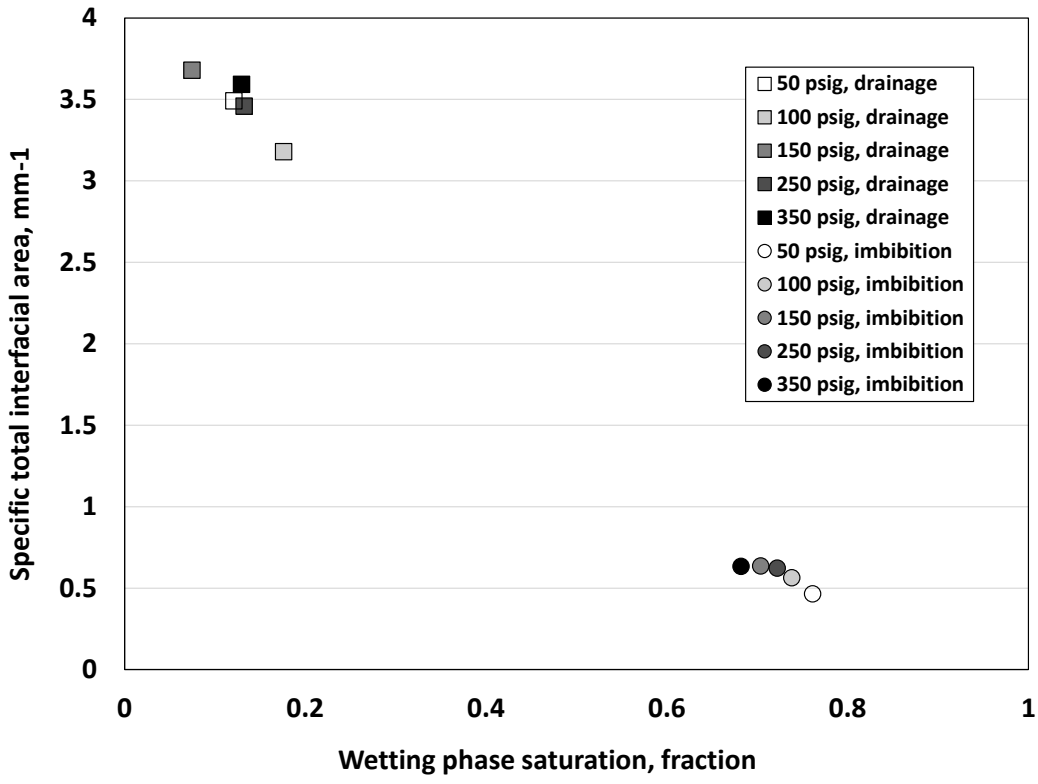

Figure 5.10 Specific total interfacial areas as a function of wetting-phase saturation at the end of each drainage and imbibition cycle at different axial loads.

Fluid interfacial areas are significant for simulation of reactions among multiple phases and is of vital importance for some type of applications that take into account the contact between the fluid and the solid phases. For example, in matrix acidizing, though acid is not soluble in oil, the contact area that the acid has with the solid is very important from the point of view of modelling the solution of the solid. Since fluid-fluid interfacial areas are extremely difficult to calculate, these reactive transport modelling simulators may need correlations in terms of fluid surface areas. In the model, the fraction of solid surface that is exposed to the acid needs to be known but there is not an explicit way to provide these interfacial areas as they change dynamically. The difficulty arises because the fluids move within the pore space and cause fluid-fluid and fluid–solid interfacial areas to change dynamically. Due to the lack of a direct mechanism to provide this data to be used in the model as input, some kind of approximations could be done. The approach for this approximation is that fluid interfacial areas could be considered as a fraction of the total solid surface area that relates to its current saturation. By simply assuming that the specific surface areas follow saturations linearly, we can make explicit direct measurements and assist with the accuracy of surface area measurements through our experiments.

Linear approximation can be done based on solid specific surface areas and saturations using following equations proposed by Landry et al. 2011:

$$a^w = a^s \, S_w$$

$$a^n = a^s \, (1 - S_w)$$

Wetting and non-wetting phase specific surface areas were found for each drainage and imbibition cycle at different axial loads and these approximations were compared with actual findings (Figure 5.11).

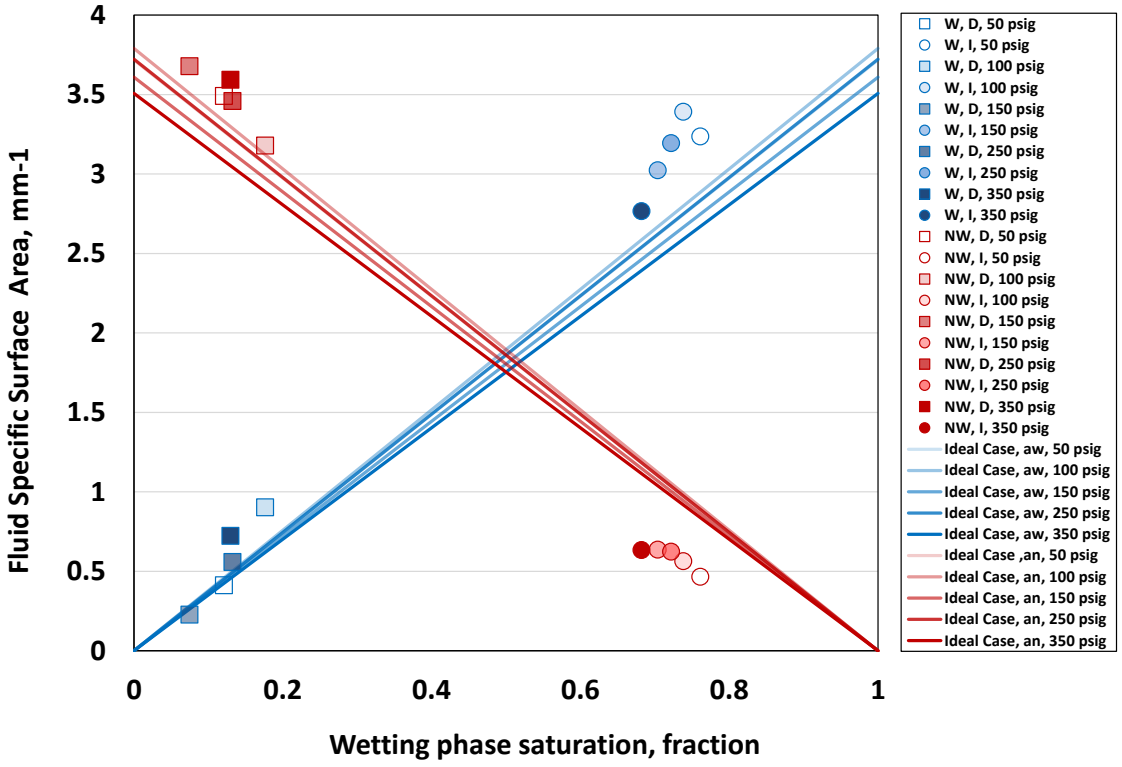

Figure 5.11 Wetting (blue) and non-wetting (red) phase specific surface areas (a_w, a_n) correspond to their saturation values. Squares represent a_w and a_n values at irreducible wetting-phase while circles are at residual non-wetting phase saturations. Solid lines are linear approximations for a_w and a_n. The shaded-in color was darkened for both symbols and lines as axial load increased.

Figure 5.11 shows the wetting and non-wetting phase specific surface areas (a^w, a^n) according to wetting-phase saturations. Solid lines represent linear approximations for a^w and a^n obtained from solid specific surface areas and saturations. Through observation we see a^w and a^n are almost in parallel with the linear approximation at the end of drainage cycles. It would appear that a^w and a^n values are not highly affected by

axial load and saturation history at low wetting-phase saturations. However, at high wetting-phase saturations, actual measurements intend to have a greater departure from that approximation. For a^w, highest deviation was observed at 100 psig axial load in both low and high wetting phase saturations. When it is compared to actual measurements, wetting-phase specific surface areas found from linear approximations seem to be underestimated at high wetting-phase saturations.

Linear approximations seem to overestimate the non-wetting phase specific surface areas at the end of imbibition while they were more accurate for drainage cycles. Again, there is not a linear trend among a^n values with respect to axial loadings. It is recognized that linear approximations are more accurate with experimental data for both wetting and non-wetting phase at irreducible wetting-phase saturations.

It could be interpreted that wetting-phase is more sensitive to variations in pore structure especially at high wetting-phase saturations. To do some type of multiphase flow analysis in a bulk porous medium depends on keeping track of that wetting-phase, having a more sensitive representation of how interfacial areas are dynamically changing. The results are partially similar to earlier experimental work presented by Landry et al. 2011 who have found deviated wetting-phase specific surface areas according to linear approximations.

Chapter 6 : Conclusions

The aim of this experimental study was to explore the impact of compaction on porosity, permeability, relative permeability, residual fluid distributions and pore-scale interfacial areas in a synthetic water-wet porous medium. In general, we did not observe a strong response in macro-scale properties according to axial loading ranging from 50 to 350 psig.

The main contribution of this work is to provide a framework to better understand effect of compaction on macro- and pore-scale properties in lab scale using X-ray microtomography. To do so, we conducted flooding experiments by injecting immiscible fluids through a glass bead packing at different axial loadings.

Our results are in agreement with the interfacial area measurements done using glass bead packings (Culligan et al. 2004; Culligan et al. 2006; Landry et al. 2011). In those studies, they reported higher meniscus interfacial areas during drainage than that of imbibition. Nevertheless, these prior studies measured the interfacial areas at different saturation points on the drainage and imbibition curves, thus implying that contact angle hysteresis was responsible for changes in meniscus interfacial area. In this study, interfacial areas were measured at residual saturations (static conditions) and a similar behavior was observed; therefore, validating the importance of saturation history on the development of final fluid distribution. Our findings provide evidence of the effects of contact angle hysteresis on pore-scale displacement mechanisms, which affect final saturation states.

More specific findings include:

a. The applied axial loading did not reveal a measurable axial compaction/deformation between 50 and 250 psig. At 350 psig, the height of the bead packing was nearly 2 mm shorter which could be inferred that the sample was axially strained at that loading. It also confirms that the beads moved within the pore space.

b. Minor changes in pore structure did not have a significant impact on macroscopic properties such as porosity and permeability but when we look at pore-scale, although changes were noticeable in terms of saturation. A slight decrease was seen in the average porosity values which confirms what was seen in absolute permeability according to axial loading. Relative permeability curves in general become more depressed with increasing axial loading.

c. Residual saturation profiles along the bead packing remained uniform at axial loadings ranging from 50 to 350 psig applied, at the end of both drainage and imbibition cycles.

d. It was noticed that wetting-phase specific surface area is more sensitive than the non-wetting to variations in pore structure at the end of imbibition. This was observed after we compare fluid surface areas with linear approximations done based on saturations and solid specific surface areas.

e. Meniscus interfacial areas were found to be higher after drainage compared to imbibition. This is most likely due to tendency of surface maximization of the wetting-phase in the water-wet medium. The wetting-phase spread out into narrow pores that might have increased meniscus interfacial area owing to its intricate structure after drainage. Moreover, it is evident that a minor change in axial strain provides more crevices, pore throats and narrow pores which the wetting-phase most likely prefer to reside. It can be said that meniscus interfacial areas are highly driven by the pore structure. It was also observed that topology of wetting and non-wetting fluid blobs plays an important role to determine wettability. Furthermore, meniscus interfacial areas at irreducible wetting-phase saturations are found to be more sensitive to variations in pore structure than that of at residual non-wetting phase saturations.

In the future, it would be beneficial to test higher axial loads to exert compaction on bead packing. It is also advised that sufficient radial stress should be applied on the bead packing to compensate for the axial loadings. Care should be taken while determining percentage of NaI used in distilled water such that 6% was found to be of limited benefit to enhance the differentiation between the solid glass and the brine phase through X-ray microtomography at the selected energy settings. Our data are expected to serve as validation tool for pore-scale numerical simulations of coupled flow and mechanical deformation.

References

Alpak, F.O. et al., 1999. Validation of a Modified Carman-Kozeny Equation To Model Two-Phase Relative Permeabilities. *SPE Annual Technical Conference and Exhibition*, pp.1–11.

Al-Raoush, R.I. & Willson, C.S., 2005. A pore-scale investigation of a multiphase porous media system. *Journal of contaminant hydrology*, 77(1-2), pp.67–89.

Avizo Guide, 2013. Avizo ® 8.

Bandara, U.C. et al., 2013. Smoothed particle hydrodynamics pore-scale simulations of unstable immiscible flow in porous media. *Advances in Water Resources*, 62, pp.356–369.

Blunt, M., 2001. Flow in porous media—pore-network models and multiphase flow. *Current opinion in colloid & interface science*, 6(3), pp.197–207.

Blunt, M.J. et al., 2013. Pore-scale imaging and modelling. *Advances in Water Resources*, 51, pp.197–216.

Boek, E.S. & Venturoli, M., 2010. Lattice-Boltzmann studies of fluid flow in porous media with realistic rock geometries. *Computers and Mathematics with Applications*, 59(7), pp.2305–2314.

Bultreys, T., Van Hoorebeke, L. & Cnudde, V., 2015. Multi-scale, micro-computed tomography-based pore network models to simulate drainage in heterogeneous rocks. *Advances in Water Resources*, 78, pp.36–49.

Chen, D. et al., 2007. Measurement of interfacial area per volume for drainage and imbibition. *Water Resources Research*, 43(12), pp.1–6.

Culligan, K. a. et al., 2004. Interfacial area measurements for unsaturated flow through a porous medium. *Water Resources Research*, 40(12), pp.1–12.

Culligan, K.A. et al., 2006. Pore-scale characteristics of multiphase flow in porous media: A comparison of air-water and oil-water experiments. *Advances in Water Resources*, 29(2), pp.227–238.

Dalla, E., Hilpert, M. & Miller, C.T., 2002. Computation of the interfacial area for two-fluid porous medium systems. *Journal of Contaminant Hydrology*, 56(1-2), pp.25–48.

Dutta, R. et al., 2013. Experimental investigation of fracturing fluid migration due to spontaneous imbibition in fractured low permeability sands. *SPE Reservoir Evaluation & Engineering*, 17(1), pp.74–81.

Geertsma, J., 1973. Land Subsidence Above Compacting Oil and Gas Reservoirs. *Journal of Petroleum Technology*, 25.

Georgiadis, a. et al., 2013. Pore-scale micro-computed-tomography imaging: Nonwetting-phase cluster-size distribution during drainage and imbibition. *Physical Review E - Statistical, Nonlinear, and Soft Matter Physics*, 88, pp.1–9.

Hassanizadeh, S.M. & Gray, W.G., 1993. Thermodynamic basis of capillary pressure in porous media. *Water Resources Research*, 29(10), pp.3389–3405.

Hazlett, R.D., Chen, S.Y. & Soll, W.E., 1998. Wettability and rate effects on immiscible displacement: Lattice Boltzmann simulation in microtomographic images of reservoir rocks. *Journal of Petroleum Science and Engineering*, 20(3-4), pp.167–175.

Hazlett, R.D. & Vaidya, R.N., 2002. Lattice Boltzmann simulations and contact angle hysteresis in convergent–divergent media. *Journal of Petroleum Science and Engineering*, 33(1-3), pp.161–171.

Hege, H. et al., 1997. A Generalized Marching Cubes Algorithm Based On Non-Binary Classifications.

Hilpert, M. & Miller, C.T., 2001. Pore-morphology-based simulation of drainage in totally wetting porous media. *Advances in Water Resources*, 24(3-4), pp.243–255.

Holt, R. et al., 2004. Consequences of depletion-induced stress changes on reservoir compaction and recovery. *" Gulf Rocks 2004, the 6th North America Rock Mechanics Symposium (NARMS). American Rock Mechanics Association, 2004.*, (1).

Iassonov, P., Gebrenegus, T. & Tuller, M., 2009. Segmentation of X-ray computed tomography images of porous materials: A crucial step for characterization and quantitative analysis of pore structures. *Water Resources Research*, 45(9), pp.1–12.

Jamaloei, B.Y. & Kharrat, R., 2010. Analysis of microscopic displacement mechanisms of dilute surfactant flooding in oil-wet and water-wet porous media. *Transport in Porous Media*, 81, pp.1–19.

Joekar-Niasar, V. & Majid Hassanizadeh, S., 2011. Effect of fluids properties on non-equilibrium capillarity effects: Dynamic pore-network modeling. *International Journal of Multiphase Flow*, 37(2), pp.198–214.

Karpyn, Z.T., Grader, a. S. & Halleck, P.M., 2007. Visualization of fluid occupancy in a rough fracture using micro-tomography. *Journal of Colloid and Interface Science*, 307, pp.181–187.

Karpyn, Z.T. & Piri, M., 2007. Prediction of fluid occupancy in fractures using network modeling and x-ray microtomography. I: Data conditioning and model description. *Physical Review E - Statistical, Nonlinear, and Soft Matter Physics*, 76, pp.1–13.

Karpyn, Z.T., Piri, M. & Singh, G., 2010. Experimental investigation of trapped oil clusters in a water-wet bead pack using X-ray microtomography. *Water Resources Research*, 46, pp.1–25.

Killough, J.E., 1976. Reservoir Simulation With History-Dependent Saturation Functions. *Society of Petroleum Engineers Journal*, 16(1), pp.37–48.

Landis, E.N. & Keane, D.T., 2010. X-ray microtomography. *Materials Characterization*, 61, pp.1305–1316.

Landry, C.J., 2010. SPE 141124-STU Interfacial Areas and Immiscible Fluid Structures of Oil and Water in Oil-Wet and Water-Wet Porous Media. *Proceedings SPE ATCE*, (September), pp.19–22.

Landry, C.J., Karpyn, Z.T. & Piri, M., 2011. Pore-scale analysis of trapped immiscible fluid structures and fluid interfacial areas in oil-wet and water-wet bead packs. *Geofluids*, 11, pp.209–227.

Larpudomlert, R. et al., 2013. Experimental investigation of residual saturation in mixed-wet porous media using a pore-scale approach. *Journal of Petroleum Exploration and Production Technology*, 4(2), pp.175–187.

Lenormand, R., Zarcone, C. & Sarr, a., 1983. Mechanisms of the displacement of one fluid by another in a network of capillary ducts. *Journal of Fluid Mechanics*, 135, p.337.

Li, G. et al., 2006. Modeling the formation of fluid banks during counter-current flow in porous media. *Transport in Porous Media*, 62, pp.125–138.

Marques, L.C. & Appoloni, C.R., 2015. Quantification of fluids injection in a glass-bead matrix using X-ray microtomography. *Micron*, pp.1–9.

Nagel, N.B., 2001. Compaction and subsidence issues within the petroleum industry: From Wilmington to Ekofisk and beyond. *Physics and Chemistry of the Earth, Part A: Solid Earth and Geodesy*, 26(1), pp.3–14.

Naghavi, B. & Kibbey, T.C.G., 2014. An Experimental Study of the Factors Influencing Apparent Wetting Phase Residual Saturation in Dynamically Drained Porous Media. *Transport in Porous Media*, 101, pp.149–160.

Olivier, P., Laveissière, J. & Guillonneau, N., 2005. Analysis of Multiphase Flow Behavior in Vugular Carbonates using X-Ray CT Scanning. *Petrophysics*, 46(6), pp.424–433.

Osoba, J.S. et al., 1951. Laboratory Measurements of Relative Permeability. *Journal of Petroleum Technology*, 3(2), pp.47–56.

Piri, M. & Karpyn, Z.T., 2007. Prediction of fluid occupancy in fractures using network modeling and x-ray microtomography. II: Results. *Physical Review E - Statistical, Nonlinear, and Soft Matter Physics*, 76, pp.1–11.

Porter, M.L., Schaap, M.G. & Wildenschild, D., 2009. Lattice-Boltzmann simulations of the capillary pressure-saturation-interfacial area relationship for porous media. *Advances in Water Resources*, 32(11), pp.1632–1640.

Saputelli, L. a, Dawe, R. a & Grattoni, C., 1998. Pore Scale Gravity Drainage under Different Wettabilities and Multiphase Coexistence. *Society of Petroleum Engineers*, pp.1–14.

Schlüter, S., Weller, U. & Vogel, H.J., 2010. Segmentation of X-ray microtomography images of soil using gradient masks. *Computers and Geosciences*, 36, pp.1246–1251.

Settari, a., 2002. Reservoir Compaction. *Journal of Petroleum Technology*, 54(08), 62.

Tartakovsky, A.M. & Meakin, P., 2006. Pore scale modeling of immiscible and miscible fluid flows using smoothed particle hydrodynamics. *Advances in Water Resources*, 29(10), pp.1464–1478.

Torrealba, V.A., 2014. *Pore-Scale Investigation on Compaction-Dependent Characteristics of Granular Packs and Their Impact on Multiphase Fluid Distribution*. The Pennsylvania State University, Master's thesis.

Valvatne, P.H., Blunt, M.J. & London, I.C., 2003. Predictive Pore-Scale Network Modeling. *SPE Annual Technical Conference and Exhibition. Society of Petroleum Engineers.*

Wellington, S.L. & Vinegar, H.J., 1987. X-ray computerized tomography. *Journal of petroleum technology*, 39(8), pp.885–898.

Wildenschild, D. & Sheppard, A.P., 2013. X-ray imaging and analysis techniques for quantifying pore-scale structure and processes in subsurface porous medium systems. *Advances in Water Resources*, 51, pp.217–246.